PROPAGATION OF THERMONUCLEAR FLAMES ON RAPIDLY ROTATING NEUTRON STARS: EXTREME WEATHER DURING TYPE I X-RAY BURSTS

ANATOLY SPITKOVSKY,[1] YURI LEVIN,[1] AND GREG USHOMIRSKY[2]

ABSTRACT

We analyze the global hydrodynamic flow in the ocean of an accreting, rapidly rotating, nonmagnetic neutron star in a low-mass X-ray binary during a type I X-ray burst. We use both analytical arguments and numerical simulations of simplified models for ocean burning. Our analysis extends previous work by taking into account the rapid rotation of the star and the lift-up of the burning ocean during the burst. We find a new regime for the spreading of a nuclear burning front, where the flame is carried along a coherent shear flow across the front. If turbulent viscosity is weak, the speed of flame propagation is $v_{\text{flame}} \sim (gh)^{1/2}/ft_n \sim 20$ km s^{-1}, where h is the scale height of the burning ocean, g is the local gravitational acceleration, t_n is the timescale for fast nuclear burning during the burst, and f is the Coriolis parameter, i.e., twice the local vertical component of the spin vector. If turbulent viscosity is dynamically important, the flame speed increases and reaches the maximum value, $v_{\text{flame}}^{\max} \sim (gh/ft_n)^{1/2} \sim 300$ km s^{-1}, when the eddy overturn frequency is comparable to the Coriolis parameter f. We show that, as a result of rotationally reduced gravity, the thermonuclear runaway which ignites the ocean is likely to begin on the equator. The equatorial belt is ignited at the beginning of the burst, and the flame then propagates from the equator to the poles. Inhomogeneous cooling (equator first, poles second) of the hot ashes drives strong zonal currents which may be unstable to the formation of Jupiter-type vortices; we conjecture that these vortices are responsible for coherent modulation of X-ray flux in the tails of some bursts. We consider the effect of strong zonal currents on the frequency of modulation of the X-ray flux and show that the large values of the frequency drifts observed in some bursts can be accounted for within our model combined with the model of homogeneous radial expansion. Additionally, if vortices or other inhomogeneities are trapped in the forward zonal flows around the propagating burning front, fast chirps with large frequency ranges (~ 25–500 Hz) may be detectable during the burst rise. Finally, we argue that an MHD dynamo within the burning front can generate a small-scale magnetic field, which may enforce vertically rigid flow in the front's wake and can explain the coherence of oscillations in the burst tail.

Subject headings: accretion, accretion disks — hydrodynamics — instabilities — nuclear reactions, nucleosynthesis, abundances — stars: neutron — X-rays: bursts

1. INTRODUCTION

Accreting neutron stars (NSs) in low-mass X-ray binaries (LMXBs) undergo type I X-ray bursts as a result of thermonuclear runaways in pure helium or mixed hydrogen/helium layers (Hansen & van Horn 1975; Maraschi & Cavaliere 1976; Woosley & Taam 1976; for reviews see Lewin, van Paradijs, & Taam 1995; Bildsten 1998). Spherically symmetric models of such runaways successfully explain general features of type I X-ray bursts, such as burst fluences ($\sim 10^{39}$ ergs), timescales for accretion between bursts (approximately a few hours), and burst durations (~ 10 s). However, spherically symmetric models cannot account for the lateral spreading of thermonuclear flames and its interplay with NS rotation, and recent observations have brought this issue into focus.

Since the timescale for accretion between bursts is much longer than the burst duration, it is unlikely that identical conditions exist over the whole stellar surface for the burning instability to start simultaneously (Shara 1982). Therefore, burning should start locally at some point, creating a brightness asymmetry, and spread over the entire surface of the star. As nuclear burning spreads around the

star, one would then expect to see a rotational modulation of the X-ray flux, with the frequency of the modulation equal to that of the NS spin. Such highly coherent ($Q \sim$ few thousand) "burst oscillations" have indeed been observed with *RXTE* in nine different bursters for many bursts with rise times of less than 1 s (see van der Klis 2000 for a review and Muno et al. 2001 for the most recent tally). The inferred NS spins v_s are between 250 and 650 Hz.

The discovery of burst oscillations, while confirming the basic expectations of millisecond spins of accreting NSs and asymmetry of nuclear burning, has brought about a host of new questions. Firstly, burst oscillations are seen only from some of the ~ 50 known Galactic LMXBs, and only some bursts from the same source show oscillations. For NSs with $v_s \sim 600$ Hz, oscillations are seen only during strong bursts with photospheric radius expansion, while for $v_s \sim 300$ Hz, oscillations are equally as likely to be seen during weak or strong bursts (Muno et al. 2001). Secondly, oscillations are most commonly seen during *tails* of bursts, when, presumably, the entire accreted fuel layer has been burned and the obvious asymmetry is no longer present. Finally, the frequency of burst oscillations drifts upward by $\Delta v \sim$ several Hz during the burst.

A simple model for the drift of the burst oscillation frequency has been proposed by Strohmayer et al. (1997) and recently considered quantitatively by Cumming & Bildsten (2000) and Cumming et al. (2002). Since the vertical sound

[1] Astronomy Department and Theoretical Astrophysics Center, 601 Campbell Hall, University of California, Berkeley, CA 94720; anatoly@astron.berkeley.edu, yurlev@astron.berkeley.edu.
[2] Theoretical Astrophysics, M/C 130-33, California Institute of Technology, Pasadena, CA 91125; gregus@tapir.caltech.edu.

crossing time through the burning layer (microseconds) is much smaller than the nuclear burning time (greater than a fraction of a second) on which the burst evolves, the outer layers of the NS are always in hydrostatic balance. When the burning layer is hot, it expands hydrostatically by $\Delta z \sim$ tens of meters while conserving angular momentum and, hence, lags behind the NS by $\Delta v / v_s \approx 2 \Delta z / R$. During the tail of the burst, a postulated temperature inhomogeneity gives rise to oscillations, and, as the layer cools down and contracts, we observe an upward frequency drift by Δv of a few Hz, roughly consistent with observations. However, recent works by van Straaten et al. (2001), Galloway et al. (2001), Wijnands, Strohmayer, & Franco (2001), and Cumming et al. (2002) suggest that purely radial hydrostatic expansion may not be sufficient to explain rather large Δv-values observed in some bursts (see discussion in § 4.3).

It has long been expected that NSs in LMXBs are progenitors of millisecond radio pulsars (for a review see Bhattacharya 1995). Detection of burst oscillations has certainly bolstered the idea that accreting NSs can reach periods similar to those seen in millisecond radio pulsars. However, except for one source, there is no convincing evidence of millisecond pulsar–like $\sim 10^9$ G magnetic fields in LMXBs. Only SAX J1808.4−365 (Wijnands & van der Klis 1998; Chakrabarty & Morgan 1998) shows coherent $v_s = 401$ Hz pulsations in persistent emission, which is consistent with the fact that a 10^8–10^9 G magnetic field channels accretion onto magnetic polar caps and creates a permanent brightness asymmetry on the NS (Psaltis & Chakrabarty 1999; though, since persistent flux modulation is only a few percent, a weaker field could perhaps be sufficient). None of the other LMXBs show such pulsations in persistent emission, implying that, if they do have magnetic fields, they must be weaker than at least 10^9 G. Moreover, the presence of frequency drifts during bursts may place even more stringent constraints on the magnetic field. If the radial lift-up model described above were correct, it would imply that the ocean and atmosphere of the NS can make up to $t_{burst} \Delta v \sim$ 10 revolutions around its interior. The magnetic field, if present in the shearing layer, will be amplified by the shear. A simple estimate (Cumming & Bildsten 2000) shows that even an $\approx 10^6$ G magnetic field might be dynamically important in this situation. Throughout this work, we neglect the dynamical effects of the NS magnetic field and only briefly discuss possible MHD effects at the end.

In this paper we abandon the requirement of spherical symmetry and consider instead the two-dimensional spreading of the nuclear fire around the NS surface. We study hydrodynamic flows that arise in the burning ocean due to the combination of its inhomogeneous lift-up and the rotation of the star. We analyze how these flows affect the spreading of fire around the NS surface. First we consider the local conditions around the flame front at the interface between the hot, burned ashes and cold, unburned fuel, exposing the nontrivial effects of rotation and viscosity on the propagation of the flame front. Armed with the understanding of local conditions, we then construct a global scenario for X-ray bursts.

The burning front during type I X-ray bursts can propagate either by deflagration (Fryxell & Woosley 1982b; Hanawa & Fujimoto 1984; Bildsten 1995) or by detonation (Fryxell & Woosley 1982a; Zingale et al. 2001). Detonation is possible when the timescale for nuclear burning is less than the vertical sound crossing time. This requires a large column of accumulated fuel (~ 100 m) before the runaway starts and, hence, rather low accretion rates of $\lesssim 10^{-11.5}$ $M_\odot$ yr^{-1}, i.e., 1–2 orders of magnitude less than the observed accretion rates in most bursters. However, direct numerical simulations of the type performed by Fryxell & Woosley (1982a) and especially by Zingale et al. (2001), if extended into the parameter regime relevant for most of the observed sources (i.e., higher accretion rate and, hence, deflagration rather than detonation), are the only definitive way to model X-ray bursts.

In most bursts, the helium/hydrogen ocean burns by spreading of a deflagration front; its propagation speed is set by the rate of heat transport across the front. Fryxell & Woosley (1982b) argue that in bursts with quick (less than 1 s) rise, which are of most interest to us, heat is conducted sideways by convection. They give three different phenomenological estimates of the speed of the front (see eqs. [3] and [4] and the bottom line of the left column on page 333 of their paper):

1. The width of the front is equal to the length scale of a convective roll, taken to be approximately the scale height h. The front speed is then

$$v_{\text{flame}} \sim \frac{h}{t_n} = 10^4 \text{ cm s}^{-1} \left(\frac{h}{10^3 \text{ cm}}\right)\left(\frac{0.1s}{t_n}\right), \qquad (1)$$

where t_n is the timescale of nuclear burning during the burst. This estimate is based on the earlier work of Ruderman (1981).

2. Heat is transported by turbulent convective diffusion, with a kinetic diffusion coefficient $D = h v_c$, where v_c is the characteristic convective speed. The front speed is then

$$v_{\text{flame}} \sim \sqrt{D/t_n} = 2 \times 10^5 \text{ cm s}^{-1}$$
$$\times \left[\left(\frac{h}{10^3 \text{ cm}}\right)\left(\frac{v_c}{5 \times 10^6 \text{ cm s}^{-1}}\right)\left(\frac{0.1s}{t_n}\right)\right]^{1/2} . \quad (2)$$

3. The turbulence scale is much larger than the front width, in which case the burning front becomes wrinkled, accelerating heat transport. In this case (Williams 1965)

$$v_{\text{flame}} \sim v_c \sim 5 \times 10^6 \text{ cm s}^{-1} . \qquad (3)$$

Cases 1 and 2, with typical expected $t_n \sim 0.1$ s, $h \sim 10^3$ cm, and $v_c \sim 5 \times 10^6$ cm s^{-1}, give burst rise times longer than the ones observed. Case 3 is, as Fryxel & Woosley (1982a) argue, the upper limit for the front velocity, but it seems that it is the only one of the three estimates which can account for the observed short rise times of bursts.

In this paper we present a new mode of heat transport across the front which does not depend on a large turbulence scale and on wrinkling of the front and can also explain the observed short rise times of type I X-ray bursts. The hot, burned ashes have a larger scale height than the cold fuel. This vertical lift-up of the ocean as the flame propagates around the star leads to a horizontal pressure gradient. Previous work (Strohmayer et al 1997; Cumming & Bildsten 2000) only considered the situation in which the entire ocean is burned and has lifted up, and, hence, the horizontal pressure balance is already restored. We argue that, as the thermonuclear flame propagates around the star, the lift-up of the ocean behind the front drives a differential shear across the front. This shear transports entropy from the hot ashes to the fuel and, hence, propagates the

front. The speed of the flame depends on the strength of the frictional coupling (e.g., due to convection) between the different layers (from top to bottom) of the burning ocean.

In § 2 we estimate analytically the following:

1. In the case of the weak frictional top-bottom coupling, the width of the front Δ is given by the Rossby adjustment radius a_R:

$$\Delta \sim a_R = \frac{\sqrt{gh_{hot}}}{f}$$

$$= 2 \text{ km} \left[\left(\frac{g}{2 \times 10^{14} \text{ cm s}^{-2}}\right)\left(\frac{h_{hot}}{10^3 \text{ cm}}\right)\right]^{1/2}$$

$$\times \left(\frac{2000 \text{ rad s}^{-1}}{f}\right), \qquad (4)$$

where g is the gravitational acceleration at the NS surface, h_{hot} is the scale height of the burned ocean, and $f = 2\Omega \cos \theta$ is the local Coriolis parameter (Ω is the angular frequency of the NS and $\pi/2 - \theta$ is the latitude). The speed of the front is

$$v_{flame} \sim \frac{\Delta}{t_n} = \frac{\sqrt{gh_{hot}}}{ft_n}$$

$$= 2 \times 10^6 \text{ cm s}^{-1} \left(\frac{\Delta}{2\text{km}}\right)\left(\frac{0.1\text{s}}{t_n}\right), \qquad (5)$$

which gives a rise time of ~ 0.7 s for burning to spread from the equator to the poles (see eq. [24]).

2. Let t_{fr} be the timescale of frictional coupling between the top and the bottom of the ocean; $t_{fr} \sim h_{hot}/v_c$ if the layers of the ocean are dynamically coupled by convection. If the coupling is strong, i.e., $t_{fr} \lesssim t_n$, friction modifies the structure of the burning front and its propagation speed. Maximum speed is reached when $t_{fr} \approx 1/f$ and is given by

$$v_{flame}^{max} \sim \left(\frac{gh_{hot}}{ft_n}\right)^{1/2}$$

$$= 3 \times 10^7 \text{ cm s}^{-1}$$

$$\times \left[\left(\frac{h_{hot}}{10^3 \text{ cm}}\right)\left(\frac{2000 \text{ rad s}^{-1}}{f}\right)\left(\frac{0.1\text{s}}{t_n}\right)\right]^{1/2} \qquad (6)$$

(eq. [34] gives the expression for the burning front speed when the frictional coupling strength is arbitrary). The burst rise time is ~ 0.1 s in this case.

In § 3 we set up and solve numerically a two-layer shallow water model which contains the essential physics of how a stably stratified ocean responds to inhomogeneously applied heating. We use this two-layer model to simulate ignition and propagation of the deflagration front, for both weak and strong frictional coupling. Our simulations are in agreement with the analytical estimates of the front speed in § 2. The shallow water model also provides us with the theoretical estimate of the size of the initial ignition spot on the NS surface. However, we are unable to determine the strength of friction from the first principles, and we leave it as a free parameter of our model. Hopefully, future direct numerical simulations will address this issue.

Armed with our understanding of flame propagation, in § 4 we set out to construct a global scenario for X-ray bursts. We argue that, as a result of rotationally reduced gravity, the thermonuclear runaway is likely to begin in the equatorial region. We then show that, as a result of the

reduced Coriolis parameter at the equator, the flame propagates faster along the equator than away from the equator. Thus, a possibly inhomogeneous equatorial belt is ignited at the beginning of the burst rise, and the flame proceeds to burn from the equator to the poles. Inside the burning front there are strong zonal currents going forward relative to the star's rotation, and there are weaker backward zonal flows in the cooling wake of the front. A burning inhomogeneity observed as a flux modulation during the burst will be trapped in the backward zonal flows, thus the observed modulation frequency is smaller than the NS spin. As the ocean cools, the zonal flow slows down, and the modulation frequency asymptotes to the NS spin frequency. This scenario for the burst frequency drift is an extension of the radial lift-up scenario proposed by Strohmayer et al. (1997) as modeled in detail by Cumming & Bildsten (2000).

We speculate that differential zonal currents can be unstable to the formation of vortices of the type observed in the atmospheres of giant planets. These vortices may be the cause of oscillations in the X-ray flux in the tail of the burst. In addition, if there are vortices trapped in the strong forward zonal currents in the burning front, we expect to see a chirp with a large frequency span (~ 25–500 Hz) during the rise of the burst. Finally, we also suggest that the burning front may generate, via an MHD dynamo, a magnetic field $B \sim 10^9$ G, with the ocean scale height as the characteristic coherence length. This magnetic field can quench the vertical shear in the backward zonal flow and thus may be responsible for the observed coherence of burst oscillations in the burst tail.

2. PROPAGATION OF THE FLAME: ANALYTICAL ARGUMENTS

2.1. Vertical Force Balance

During the burst, the burning material reaches temperatures of $\sim 2 \times 10^9$ K, degeneracy in the helium layer is lifted, and the burning ocean expands by 10–40 m, many scale heights of the cold preburst ocean (Joss 1977; see Cumming & Bildsten 2000 for the most recent calculations). This vertical expansion is very subsonic. However, since only a part of the star is burning at a given time, the horizontal pressure imbalance leads to nontrivial hydrodynamic flows, as we now discuss.

Consider a propagating burning front, as illustrated in Figure 1, where the ocean behind the burning front is already hot, while the ocean ahead of the front is still cold.
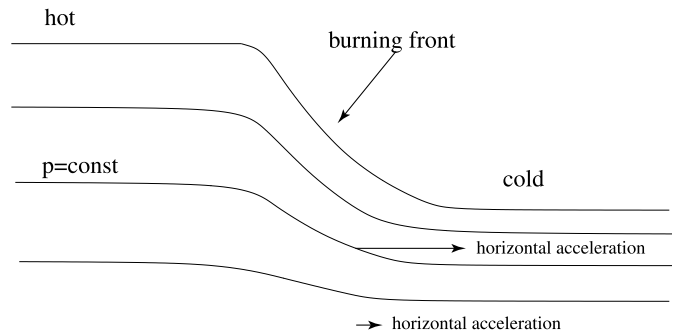

FIG. 1.—Illustration of a burning front moving from the hot to the cold region in the atmosphere/ocean.

Let the ocean, for simplicity, reside on a plane, with x and z being the horizontal and the vertical coordinates, respectively; z is taken to increase upward. Since the vertical sound crossing time is much smaller than the characteristic nuclear burning timescale during the burst, t_n, vertical hydrostatic equilibrium is always a good approximation (we also neglect the vertical component of the Coriolis force; see § 2.2). Therefore,

$$\left(\frac{\partial p}{\partial z}\right)_x = -g\rho , \qquad (7)$$

where $p(x, z)$ is the pressure and $\rho(x, z)$ is the density. From equation (7) we see that the separation between constant pressure surfaces scales as $1/\rho$. The hot ocean is less dense than the cold one, so the pressure surfaces diverge as they traverse the front from the cold into the hotter part (see Fig. 1). This implies that the horizontal pressure gradient $\partial p/\partial x$ (indicated by horizontal arrows in Fig. 1) increases with height inside the burning front. This difference in the horizontal pressure gradient drives a shear flow and circulation across the front.

Let us quantify the above argument. Let $\phi(x, z)$ be the effective gravitational potential per unit mass, $d\phi = g\,dz$. The horizontal[3] acceleration of a fluid element due to the pressure gradient is given by

$$a_{\text{pressure}} = -\frac{1}{\rho(x, \phi)}\left[\frac{\partial p(x, \phi)}{\partial x}\right]_\phi . \qquad (8)$$

Furthermore,

$$\left(\frac{\partial p}{\partial x}\right)_\phi = -\left(\frac{\partial p}{\partial \phi}\right)_x\left(\frac{\partial \phi}{\partial x}\right)_p = \rho(x, \phi)\left(\frac{\partial \phi}{\partial x}\right)_p . \qquad (9)$$

Therefore, from equations (8) and (9), we have

$$a_{\text{pressure}} = -\left(\frac{\partial \phi}{\partial x}\right)_p . \qquad (10)$$

Equation (10) is easy to understand: the height ϕ/g of surfaces of constant pressure decreases from the hot to the cold part of the ocean, so a_{pressure} is directed from the hot region to the cold region (arrows in Fig. 1). Differentiating equation (10) with respect to $\ln p$ at constant x and using equation (7), we get

$$\left(\frac{\partial a_{\text{pressure}}}{\partial \ln p}\right)_x = -p\left(\frac{\partial}{\partial x}\right)_p\left(\frac{\partial \phi}{\partial p}\right)_x$$
$$= \left[\frac{\partial(p/\rho)}{\partial x}\right]_p = \left[\frac{\partial(c_s^2/\gamma)}{\partial x}\right]_p , \qquad (11)$$

where c_s is the speed of sound and γ is the adiabatic index of the gas. As an example, for an ideal chemically homogeneous gas

$$\frac{\partial a_{\text{pressure}}}{\partial \ln p} = \frac{R}{\mu}\left(\frac{\partial T}{\partial x}\right)_p , \qquad (12)$$

where T is the temperature and μ is the mean molecular weight of the gas. The term on the right-hand side of equation (12) is the forcing term for the vertical shear; it is determined by the horizontal temperature gradient.

---

[3] A horizontal surface is a surface of constant ϕ; in plane-parallel geometry with constant g, setting $\phi = \text{const}$ is equivalent to $z = \text{const}$.

2.2. Horizontal Force Balance and Flame Propagation in the Ocean without Friction

Let us now write down the horizontal momentum equation. In a frame rotating with the star, a fluid element moving with velocity v experiences the Coriolis acceleration, $a_{\text{Coriolis}} = -2\Omega \times v$, where Ω is the angular velocity of the star. In general, the Coriolis vector 2Ω has both vertical and horizontal components in the local frame of the ocean. In what follows we shall neglect the horizontal component of the Coriolis vector (this is commonly known as the "traditional approximation" in geophysics; see, e.g., Pedlosky 1987). In doing so, we neglect two terms in the momentum equation. First, in the equation for the vertical force balance (§ 2.1) we neglect the vertical component of the Coriolis force due to horizontal motion, $\sim \Omega v$. As we shall see below, $v_{\text{max}} \sim (gh)^{1/2}$, so this component of the Coriolis force is negligible compared to gravity so long as $\Omega \ll (g/h)^{1/2} = 4 \times 10^5(h/10^3\text{cm})^{-1/2}$, which is always satisfied for NSs in LMXBs. Second, we neglect the horizontal component of the Coriolis force due to radial motion, $\sim \Omega v_z$, which is small compared to the horizontal Coriolis force due to horizontal motion, $\sim \Omega v$. This can be seen as follows: during the burst, the ocean expands vertically on the nuclear timescale t_n, and the vertical velocity is $v_z \sim h/t_n$. Therefore, the horizontal Coriolis acceleration due to radial motion is much less then the horizontal Coriolis acceleration due to horizontal motion so long as $1/t_n \ll (g/h)^{1/2}$. This condition is always satisfied for type I X-ray bursts.

With the above approximations, and in the absence of viscosity (this assumption is alleviated in § 2.3), the horizontal force balance is

$$a_{\text{pressure}} = \frac{dv}{dt} + f \times v , \qquad (13)$$

where v is the horizontal component of the velocity and $f = 2\Omega \cos \theta \hat{z}$ is the vertical Coriolis vector.

Accreting NSs which display type I X-ray bursts are typically spinning with frequencies v_s of a few hundred Hz. The characteristic timescales of the burst light curves are orders of magnitude greater than the rotation period of the NS: a typical burst rise time is 0.1–1 s, and a typical burst cooling time is 5–100 s. Theoretical calculations (see Bildsten 1998 for a review) suggest that the nuclear burning timescale during a typical burst is $t_n \sim 0.1$ s, still much greater than $1/v_s$. Therefore, during the burst the ocean flow must be in quasi-geostrophic equilibrium (Pedlosky 1987) everywhere except for the immediate vicinity of the equator. Quasi-geostrophic equilibrium implies that inertial external forces acting on a fluid element in the horizontal direction (in particular, due to the horizontal pressure gradient) are almost exactly balanced by the horizontal component of the Coriolis force.

One can see this by noting that the second term on the right-hand side of equation (13) is dominant. We can rewrite this equation as

$$v = -\frac{1}{f^2}f \times a_{\text{pressure}} + \frac{1}{f^2}f \times \frac{dv}{dt} . \qquad (14)$$

To zeroth order,

$$v = v_{\text{geostrophic}} = -\frac{1}{f^2}f \times a_{\text{pressure}} . \qquad (15)$$

Substituting this expression into the right-hand side of equation (14), we get the first-order correction to the velocity:

$$v = v_{\text{geostrophic}} + v_{\text{ageostrophic}}$$

$$= -\frac{1}{f^2} f \times a_{\text{pressure}} + \frac{1}{f^2} \frac{da_{\text{pressure}}}{dt}. \quad (16)$$

The first term in equation (16) represents the dominant geostrophic flow in the direction along the front line and perpendicular to the pressure gradient. The second term is the ageostrophic component of the velocity, which is perpendicular to the front line. Differentiating equation (16) with respect to $\ln p$ and using equation (12), we get

$$\frac{\partial v_{\text{geostrophic}}}{\partial \ln p} = -\frac{1}{f^2} f \times \frac{\partial(p/\rho)}{\partial x} \quad (17)$$

and

$$\frac{\partial v_{\text{ageostrophic}}}{\partial \ln p} = \frac{1}{f^2} \frac{\partial}{\partial \ln p} \frac{da_{\text{pressure}}}{dt}. \quad (18)$$

Equation (17) is commonly referred to as the thermal wind relation in the meteorology/geophysics literature. It implies that the difference in geostrophic velocity $\delta v_{\text{geostrophic}}$ between the top and the bottom of the ocean somewhere in the middle of the front is related to the difference in p/ρ between the hot and the cold parts of the ocean:

$$\delta v_{\text{geostrophic}} = v_{\text{geostrophic}}^{\text{top}} - v_{\text{geostrophic}}^{\text{bottom}}$$

$$\sim \frac{(p/\rho)_{\text{hot}} - (p/\rho)_{\text{cold}}}{f\Delta} \approx \frac{gh_{\text{hot}}}{f\Delta}, \quad (19)$$

where h_{hot} is the scale height of the ocean behind the front which has just undergone a thermonuclear runaway, Δ is the width of the front, and we used the fact that $h_{\text{hot}} \gg h_{\text{cold}}$.

Likewise, we can use equation (18) to estimate the characteristic ageostrophic shear $\delta v_{\text{ageostrophic}} = v_{\text{ageostrophic}}^{\text{top}} - v_{\text{ageostrophic}}^{\text{bottom}}$ somewhere in the middle of the front. Since the front passes through a given fluid element on the timescale of order t_n, we replace d/dt by $1/t_n$ in our order-of-magnitude estimates. Then

$$\frac{\partial v_{\text{ageostrophic}}}{\partial \ln p} = \delta v_{\text{ageostrophic}} \sim \frac{1}{f^2 t_n} \frac{\partial a_{\text{pressure}}}{\partial \ln p} \sim \frac{gh_{\text{hot}}}{f^2 t_n \Delta} \hat{n}. \quad (20)$$

Here $\hat{n}$ is the unit vector perpendicular to the front line.

The quantity $\delta v_{\text{ageostrophic}}$ is the characteristic speed of the shear flow perpendicular to the burning front. How does it relate to the flame propagation speed? Generally, flames propagate by transporting entropy from the hot, burned material to the cold, unburned fuel, and their speed is set by the time it takes to transport this heat across the width of the front. In the case of slow, laminar deflagration fronts (see, e.g., Bildsten 1995) heat is transported by conduction, while for convective fronts discussed by Fryxell & Woosley (1982b), heat is advected by the turbulent motion of the fluid and then mixed into the fuel. In our case, however, it is the shear flow, $\delta v_{\text{ageostrophic}}$, that moves the hot material ahead of the front (this happens at the top of the burning ocean) and pulls the cold fresh fuel into the burning front (this happens at the bottom of the ocean).

We assume that vertical mixing occurs within the front and that this mixing transports heat between the hot burning fluid moving forward on the top and the cold fluid on the bottom. This mixing could be due to either convection or various shear instabilities. Indeed, one-dimensional numerical simulations, starting with Joss (1977), show that X-ray bursts are strongly convective, with a convective overturn timescale of $\sim 10^{-3}$ s. If convection is present within the front, it will efficiently mix entropy in the vertical direction. However, while in one dimension the hot burned fluid has no place to go but to mix with the cold unburned fuel, in more than one dimension convection may be quenched by the sideways propagation of the hot material on top of the cold material.[4] In addition to the possibility of convection, the geostrophic flow within the front possesses strong vertical shear, with velocity difference of $\delta v \sim (gh_{\text{hot}})^{1/2}$ across a scale height (see eqs. [17] and [25]), which corresponds to the Richardson number of order unity. The front with such strong shear may be unstable to the Kelvin-Helmholtz instability. Finally, the interface between the shearing layers is not exactly horizontal but has a slope of order $h_{\text{hot}}/\Delta \lesssim 10^{-2}$. Such flow may be unstable to the baroclinic instability (Fujimoto 1988; Cumming & Bildsten 2000). The nonlinear development of these or other instabilities might result in efficient vertical mixing. The presence of efficient vertical mixing within the front is the most uncertain part of our model; it must be addressed directly by future numerical simulations. However, given the large amount of shear in the burning front, such mixing is not at all unreasonable.

We therefore believe that the vertical thermal mixing timescale t_{mixing} within our geostrophic front is much smaller than t_n (e.g., the convective overturn timescale is 10^{-3} s). In the foregoing, we assume that the entropy advected forward by the ageostrophic flow is quickly mixed in the vertical direction. If the thermal mixing timescale t_{mixing} within the front is nonnegligible, then the general argument laid out in this paper is unchanged, except that all estimates should use $t_n + t_{\text{mixing}}$ instead of just t_n.

If entropy mixing is efficient, then the front propagation speed is the velocity with which entropy is transported, i.e., the characteristic speed of the ageostrophic shear flow:

$$v_{\text{flame}} \sim \delta v_{\text{ageostrophic}} \sim \frac{gh_{\text{hot}}}{f^2 t_n \Delta}. \quad (21)$$

The width of the propagating front is (e.g., Fryxell & Woosley 1982b)

$$\Delta \sim v_{\text{flame}} t_n. \quad (22)$$

Substituting this into equation (21) and solving for the front speed and width, we get

$$v_{\text{flame}} \sim \frac{(gh_{\text{hot}})^{1/2}}{ft_n}$$

$$\approx 20 \text{ km s}^{-1} \left(\frac{h_{\text{hot}}}{10^3 \text{ cm}}\right)^{1/2} \left(\frac{2000 \text{ rad s}^{-1}}{f}\right)$$

$$\times \left(\frac{0.1 \text{ s}}{t_n}\right) \quad (23)$$

---

[4] We thank Lars Bildsten and Andrew Cumming for making this point.

and

$$\Delta \sim \frac{(gh_{\rm hot})^{1/2}}{f} \approx 2 \text{ km} \left(\frac{h_{\rm hot}}{10^3 \text{ cm}}\right)^{1/2}\left(\frac{2000 \text{ rad s}^{-1}}{f}\right) \quad (24)$$

for $g = 2 \times 10^{14}$ cm s^{-2}. From equation (19) the characteristic geostrophic velocity inside the front is of order the gravity wave speed in the hot material:

$$v_{\rm geostrophic} \approx (gh_{\rm hot})^{1/2} . \quad (25)$$

Note that the width of the front is equal, to the order of magnitude, to the Rossby adjustment radius (Pedlosky 1987).

2.3. Horizontal Force Balance and Flame Propagation in the Ocean with Friction

In the previous subsection we have assumed that there are no viscous forces acting on fluid elements and hence that the top and the bottom of the burning ocean are free to slip past each other. However, there is likely to be some vertical mixing within the front, as a result of turbulence driven by convection or by strong shear (see the discussion in the previous subsection). This mixing will exchange momentum between the top and the bottom of the ocean; we must, therefore, consider what effect viscous-type friction within the ocean will have on the propagation of the burning front.

Let us return to the horizontal force balance equation (13) and include viscosity:

$$a_{\rm pressure} = \frac{dv}{dt} + f \times v - a_{\rm viscous} , \quad (26)$$

where we have added to the right-hand side the acceleration of the fluid element due to viscous stress. We now consider the difference in $a_{\rm pressure}$ between the bottom and the top of the burning ocean, where we take the top to be roughly 1 scale height above the bottom. From the previous equation we have

$$a_{\rm pressure}^{\rm top} - a_{\rm pressure}^{\rm bottom} = \frac{dv_{\rm top}}{dt} - \frac{dv_{\rm bottom}}{dt}$$
$$+ f \times (v_{\rm top} - v_{\rm bottom})$$
$$- (a_{\rm viscous}^{\rm top} - a_{\rm viscous}^{\rm bottom}) . \quad (27)$$

We assume that effective viscosity dynamically couples the top and the bottom of the burning ocean and model this coupling by introducing a linear friction term:

$$a_{\rm viscous}^{\rm top} - a_{\rm viscous}^{\rm bottom} = -\frac{1}{t_{\rm fr}} (v_{\rm top} - v_{\rm bottom}) . \quad (28)$$

If friction is mediated by turbulent eddies, then $1/t_{\rm fr} = \beta_1 v_{\rm turb}/h$, where $v_{\rm turb}$ is the characteristic velocity of the largest turbulent eddy and β_1 is a number of order unity. On the left-hand side of equation (27) we use equation (12) to get

$$a_{\rm pressure}^{\rm top} - a_{\rm pressure}^{\rm bottom} \sim \frac{da_{\rm pressure}}{d \ln p} \sim \left[\frac{\partial (p/\rho)}{\partial x}\right]_p \sim g \frac{h_{\rm hot}}{\Delta} \hat{n} . \quad (29)$$

Finally, as in § 2.2, we replace in equation (27) the time derivative d/dt by η/t_n, where η is a number of order unity. With the above simplifications, the shear flow $\delta v = v_{\rm top}$

$- v_{\rm bottom}$ obeys

$$g \frac{h_{\rm hot}}{\Delta} \hat{n} \sim \left[f \times \delta v + \left(\frac{1}{t_{\rm fr}} + \frac{\eta}{t_n}\right)\delta v\right] . \quad (30)$$

Scalar multiplication of the above equation by δv yields

$$g \frac{h_{\rm hot}}{\Delta} (\delta v \cdot \hat{n}) \sim \left(\frac{1}{t_{\rm fr}} + \frac{\eta}{t_n}\right)(\delta v)^2 , \quad (31)$$

while application of the Pythagorean theorem to equation (30) yields

$$(\delta v)^2 \sim \left(\frac{gh_{\rm hot}}{\Delta}\right)^2 \frac{1}{f^2 + (1/t_{\rm fr} + \eta/t_n)^2} . \quad (32)$$

Therefore, the component of the shear flow across the front is just

$$\delta v \cdot \hat{n} \sim \frac{gh_{\rm hot}(1/t_{\rm fr} + \eta/t_n)}{[f^2 + (1/t_{\rm fr} + \eta/t_n)^2]\Delta} . \quad (33)$$

As argued in § 2.2, the speed of the front is determined by the speed of the shear flow across the front line, i.e., $v_{\rm flame} \sim \delta v \cdot \hat{n}$. Then, using $\Delta \sim v_{\rm flame} t_n$ in equation (33), we get

$$v_{\rm flame} \sim \left[\frac{gh_{\rm hot}}{t_n} \frac{1/t_{\rm fr} + \eta/t_n}{f^2 + (1/t_{\rm fr} + \eta/t_n)^2}\right]^{1/2} . \quad (34)$$

The typical parameter values relevant for the burning ocean are $g = 2 \times 10^{14}$ cm s^{-2}, $h_{\rm hot} = 10^3$ cm, $t_n = 0.1$ s, and $f = 2000$ rad s^{-1}. For purposes of illustration, we take the eddy velocity to be equal to the typical convective velocity inferred from one-dimensional models of X-ray bursts $v_{\rm turb} = v_c = 5 \times 10^6$ cm s^{-1} and set the frictional timescale $t_{\rm fr}$ to $h_{\rm hot}/v_{\rm turb}$. We then obtain the numerical value of $v_{\rm flame} \sim 200$ km s^{-1}. This corresponds to a burst rise time (equator to pole spreading) of ~ 0.1 s.

In Figure 2 we show the speed of the flame front $v_{\rm flame}$ as a function of the strength of the dimensionless frictional coupling constant, $(t_{\rm fr} f)^{-1}$. The filled circles represent the results of our model simulations, which are discussed in the next section. The solid line is a fit made using the functional form of equation (34) and adjusting the values of $h_{\rm hot}$ and t_n to match the simulation. The agreement between the model simulations and the analytical formula for the speed propagation is very good, which means that the analytical estimates capture the physics contained in the problem quite well.

In Figure 2, three regimes of the front speed are evident. When frictional coupling is very weak (i.e., $t_{\rm fr} \gg t_n$ and $t_{\rm fr} \gg 1/f$), the front speed asymptotes to a constant value given by equation (24), i.e., we recover the result of § 2.2 for frictionless flame propagation. When friction is important (i.e., $t_{\rm fr} \lesssim t_n$), there are two distinct regimes, depending on whether the coupling frequency $1/t_{\rm fr}$ is smaller or greater than the Coriolis parameter f. When $1/t_{\rm fr} \ll f$ (friction is small), then

$$v_{\rm flame} \sim \left(\frac{gh_{\rm hot}}{ft_n} \frac{1/t_{\rm fr} + \eta/t_n}{f}\right)^{1/2} , \quad (35)$$

while if friction is strong ($1/t_{\rm fr} \gg f$),

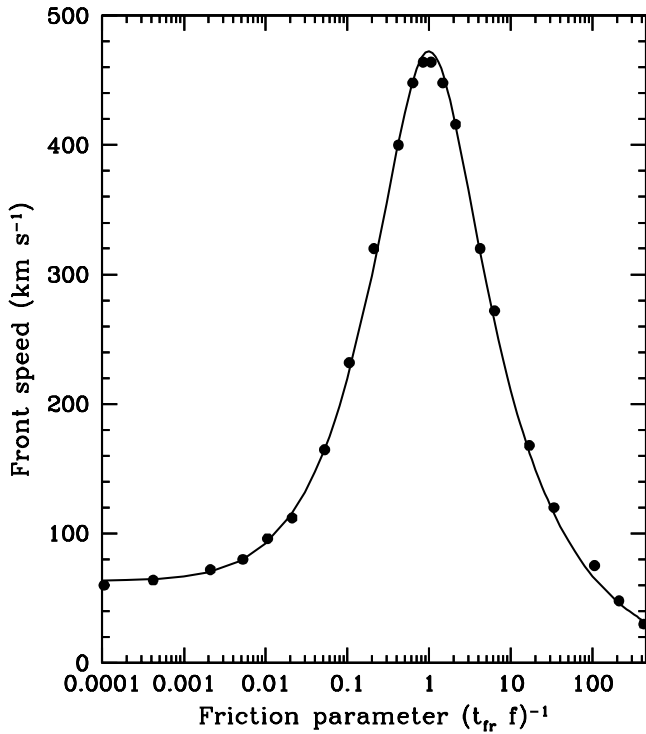$$v_{\rm flame} \sim \left(\frac{gh_{\rm hot} t_{\rm fr}}{t_n}\right)^{1/2} . \quad (36)$$

FIG. 2.—Front speed as a function of friction strength, $(t_{fr} f)^{-1}$. Filled circles represent the results of the shallow water simulation (§ 3.7), and the solid line is the fit using the analytical expression for the front speed (eq. [34], § 2.3).

For a fixed frictional coupling timescale t_{fr}, the front speed is always a decreasing function of f; for a fixed f the front speed attains a maximum value when friction is acting on the rotation timescale, $1/t_{fr} = f$:

$$v_{flame}^{max} \sim \left(\frac{gh_{hot}}{ft_n} \right)^{1/2} . \quad (37)$$

Comparison with equation (24) shows that the maximum speed is a factor of $(ft_n)^{1/2} \sim 15$ larger than the front speed without friction. The increase of the front speed when friction is introduced into the ocean can be qualitatively understood as follows. Without friction, the dominant component of the fluid velocity, $v_{geostrophic}$, is exactly parallel to the front, and the cross-front velocity, $\delta v_{ageostrophic}$, is a factor of ft_n smaller. The presence of friction modifies geostrophic balance so that the geostrophic shear flow has a component perpendicular to the front. However, if friction becomes too large, it will suppress the shear, and the front will stall. The cross-front component of geostrophic shear is maximized when friction and Coriolis force have the same magnitude, $1/t_{fr} \approx f$.

In the above analytical estimates we neglected the effect of the magnetic field that may be present on the NS surface. What is the magnitude of a B field that would have dynamical consequences? This B field would have to alter the leading-order geostrophic balance (see eqs. [13] and [26]), i.e., $B_{dynamical} \sim (4\pi\rho v_{geostrophic}^2)^{1/2}$. If viscous coupling is negligible, $v_{geostrophic} \sim (gh_{hot})^{1/2}$, and

$$B_{dynamical} \sim 10^{12} \text{ G} \left(\frac{\rho}{10^6 \text{ g cm}^{-3}} \right)^{1/2} \left(\frac{h_{hot}}{10^3 \text{ cm}} \right)^{1/2} , \quad (38)$$

i.e., magnetic energy density needs to be comparable to the hydrostatic pressure in order to affect geostrophic flow. Conversely, if convective viscosity is such that $v_{flame} = v_{flame}^{max}$, then $v_{geostrophic} \sim gh/f\Delta \sim (gh_{hot}/ft_n)^{1/2}$, and the above estimate is a factor of $(ft_n)^{1/2} \sim 15$ smaller. Even in order to affect the first-order correction to the geostrophic balance, i.e., the cross-front circulation, the magnetic pressure has to be comparable to $\rho v_{ageostrophic}^2/2$. The smallest ageostrophic velocity is attained in the case of no friction, $v_{ageostrophic} \sim (gh_{hot})^{1/2}/ft_n$ (see eqs. [21] and [24]), which still requires $B_{dynamical} \gtrsim 10^9$ G in order to affect the details of the cross-front circulation. As discussed in § 1, it is unlikely that accreting NSs in LMXBs possess surface magnetic fields of this magnitude.

The argument above applies to the instantaneous effect of magnetic field on the flow and does not take into account the nonlinear evolution of magnetic field in the (possibly turbulent) shear flow and the back-reaction of the evolved field on the flow (see, e.g., Kluzniak & Ruderman 1998; Spruit 1999; Cumming & Bildsten 2000). Detailed consideration of this issue is beyond the scope of this paper. In § 4 we only briefly speculate on magnetic field generation by an MHD dynamo in the burning front.

In the next section we construct an explicit two-layer shallow water model for flame propagation, which we designed to include the essential physics described in this section. Our numerical simulations confirm the analytical results presented here.

3. PROPAGATION OF THE FLAME: NUMERICAL MODEL

3.1. Motivation and Basic Description of the Two-Layer Model

In this section we outline one particular approach to modeling hydrodynamic flows in a stratified plane-parallel atmosphere[5] in the presence of localized heat sources and sinks (thermal forcing). The thermodynamic state of a parcel of fluid in the atmosphere will be described using its temperature, T, pressure, p, and potential temperature, $\theta = T(p_0/p)^\kappa$, where p_0 is some constant reference pressure and κ is related to the adiabatic index of the gas, γ, as $\kappa = 1 - 1/\gamma$. Potential temperature can be interpreted as the temperature which a parcel would have if it were adiabatically brought from pressure p to the reference pressure p_0 (Holton 1992). It is equal to $\exp s$, where s is the specific entropy of the parcel. In a stably stratified atmosphere potential temperature should increase or be constant with height. Another property which follows from the definition of θ is that for fixed pressure it is proportional to the specific volume of the gas: $\theta \propto (1/\rho)p^{(1-\kappa)}$. For the particular case $\kappa = 1$ which will be utilized below, potential temperature is equivalent to the specific volume of a parcel of fluid.

Now we can begin to evaluate the qualitative effects of heating on an atmospheric column. From the heat equation we have

$$\frac{d\ln\theta}{dt} = \frac{J}{c_p T} , \quad (39)$$

where J is the net rate of heating (or cooling) per unit mass, which, in our case, is the difference between the nuclear energy generation rate and the radiative cooling rate. The

---

[5] Henceforth we use the terms "atmosphere" and "ocean" interchangeably.

effect of heat input, therefore, is to change the potential temperature of the element of fluid. Such a change, coupled with maintenance of vertical hydrostatic balance in the column, leads to hydrodynamic circulation. As a simple example of how such a circulation arises, consider two columns of gas of equal column density but of different potential temperature $(\theta_1 > \theta_2)$ positioned next to each other (see Fig. 3, *left panel*). Each of the columns is assumed to be in vertical hydrostatic equilibrium. This situation can arise if column 1 is strongly heated, so that its entropy is instantly increased relative to the entropy of column 2. This configuration, however, is not stable: the fluid with higher entropy will end up on top of the fluid with lower entropy, and the atmosphere will become stably stratified (see Fig. 3, *right panel*). The dynamics of this adjustment can be qualitatively described as follows. Initially, let the tops of the columns be at the same outside pressure; the bottom pressure then will also be the same since the column densities are equal for both columns. At higher altitude the pressure in column 1 is larger than in column 2 at the same height because the density in column 1 is lower than that of column 2 (see Fig. 1). At first the fluid will flow from column 1 toward column 2 along the top, and not along the bottom where the pressures are the same. As the high-entropy fluid accumulates on top of column 2, the pressures at the bottom no longer match, and there will be a flow of fluid from column 2 toward column 1 along the bottom as well. This circulation will continue until the equilibrium state shown in the right panel of Figure 3 is achieved. Note that we assumed that this equilibration is happening adiabatically, so that the fluids of different entropy maintain their identity and in the end do not mix but stratify.

The entropy stratification described above suggests a useful analogy for the effect of a heat source in the atmosphere. Since higher entropy fluid ends up on top of the lower entropy fluid, we can treat entropy (or potential temperature) as a generalized vertical coordinate. The action of the heat source is then to pump fluid from a low entropy level to a high entropy level while conserving mass. The isentropic levels generally do not coincide with the levels of constant height, and there will be a circulation of fluid. If the motion outside the heat source is adiabatic, it is impossible for the fluid to cross the isentropic level again, and the motion will be along the isentropes.

Henceforth, we will adopt a particularly simple, yet powerful, model which uses the equation of state with $\kappa = 1$

$(\gamma \to \infty)$. The fluid with such an equation of state is quasi-incompressible: it does not allow adiabatic motions which involve compression and rarefaction and has an infinite speed of sound. However, for $\kappa = 1$, the potential temperature is equal to the specific volume of the fluid, and heating will lower the density of the fluid while conserving its mass.

Following Ooyama (1969), we consider an atmosphere consisting of two layers of incompressible fluid of different density, with density ratio $\epsilon \equiv \rho_2/\rho_1 < 1$. The lighter fluid is assumed to be in the top layer (layer 2). A fluid element is allowed to be in one of the two possible density states, ρ_1 or ρ_2. The heating is assumed to be located at the interface between the two layers (which is not necessarily a surface of constant height); the physical effect of the heating is to convert the "cold" dense material of density ρ_1 into the "hot" light material of density ρ_2, transferring the fluid from the lower (cold) to the upper (hot) layer. The equations of motion for the two layers are then given by the shallow water system of equations (Pedlosky 1987) individually formulated for each layer. The crucial distinction of our model is the interlayer coupling source/sink term in the mass continuity equation, as well as the friction between the layers:

$$\frac{\partial h_1}{\partial t} + \mathbf{\nabla}_{\|} \cdot h_1 \boldsymbol{v}_1 = -\epsilon(Q_+ - Q_-), \qquad (40)$$

$$\frac{\partial h_2}{\partial t} + \mathbf{\nabla}_{\|} \cdot h_2 \boldsymbol{v}_2 = Q_+ - Q_-, \qquad (41)$$

$$\frac{\partial v_{1x}}{\partial t} + \boldsymbol{v}_1 \cdot \mathbf{\nabla}_{\|} v_{1x} = -g\nabla_x(h_1 + \epsilon h_2) + fv_{1y}$$
$$-\frac{\epsilon}{h_1}(Q_- + \mu_f)(v_{1x} - v_{2x}), \quad (42)$$

$$\frac{\partial v_{2x}}{\partial t} + \boldsymbol{v}_2 \cdot \mathbf{\nabla}_{\|} v_{2x} = -g\nabla_x(h_1 + h_2) + fv_{2y}$$
$$-\frac{Q_+ + \mu_f}{h_2}(v_{2x} - v_{1x}), \qquad (43)$$

$$\frac{\partial v_{1y}}{\partial t} + \boldsymbol{v}_1 \cdot \mathbf{\nabla}_{\|} v_{1y} = -fv_{1x} - \frac{\epsilon}{h_1}(Q_- + \mu_f)$$
$$\times (v_{1y} - v_{2y}), \qquad (44)$$

$$\frac{\partial v_{2y}}{\partial t} + \boldsymbol{v}_2 \cdot \mathbf{\nabla}_{\|} v_{2y} = -fv_{2x} - \frac{Q_+ + \mu_f}{h_2}$$
$$\times (v_{2y} - v_{1y}) \qquad (45)$$

(cf. eqs. [3.5]–[3.7] of Ooyama 1969). Here h_1 and h_2 are the heights of the cold and hot layers, respectively. We consider the dynamics on an x-y plane with $\mathbf{\nabla}_{\|} = (\partial/\partial x, \partial/\partial y)$. To keep the problem tractable, we will allow variation only in the x-direction, so that we have a slab geometry in x with possible tangential velocity v_y. Depending on the case under consideration, the plane of the simulation will be oriented in various ways on the NS surface. The heating rate $Q \equiv J/g$ represents the flux of material from the lower to the upper layer and has dimensions of velocity (for the derivation of eqs. [40]–[41] see Appendix A). The quantities Q_+ and Q_- are defined as follows: $Q_+ = Q$, $Q_- = 0$ if the heating rate $Q > 0$, and $Q_- = -Q$, $Q_+ = 0$ if $Q < 0$. The terms on the
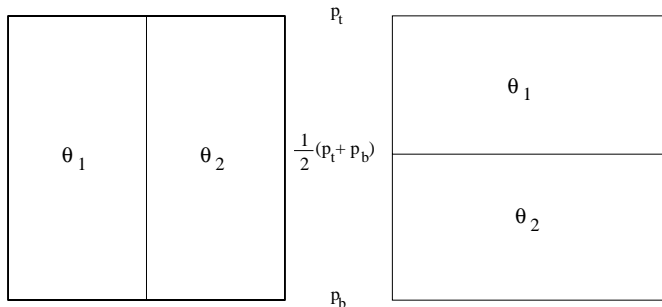

Fig. 3.—Adjustment to equilibrium in a fluid with an entropy gradient. *Left*: Initial configuration with two columns of equal mass with uniform potential temperature $\theta_1 > \theta_2$ in vertical hydrostatic balance. Upper surfaces are at the same external pressure p_t, but not at the same height. *Right*: Final configuration: entropy stratification. Higher entropy fluid is on top, and the interface is at pressure $\frac{1}{2}(p_t + p_b)$.

right-hand side of the above equations which are proportional to $\mu_f(v_1 - v_2)$ and $Q_\pm(v_1 - v_2)$ represent the friction between the two layers, the former due to (perhaps convective) viscosity and the latter due to momentum-conserving transport of material from one layer to another.

In general, the heating rate depends on the temperature at the point where the heat source is applied. Ooyama (1969) argues that for the shallow water model it is reasonable to assume that the temperature of the fluid can be represented by its height. His argument is roughly as follows: an adiabatic temperature rise in a normal fluid happens when the flow is converging, but a converging flow in a shallow water fluid results in a rise of its height. Likewise, an increase of the temperature due to heat input corresponds to addition of fluid to a shallow water layer and hence corresponds to an increase of its height. Thus, the temperature increase in a normal fluid, due to both compression and the heat input, corresponds to the height increase in a shallow water fluid. In our model we shall assume that the temperature at the interface where the heating occurs is set by the height of the second, light layer through a simple relationship $T = gh_2/c_p$.

In the following three subsections we consider how our model responds to localized sources of heat. This will help us develop intuition which will be useful in analyzing the ignition and spreading of the burning front.

3.2. Localized Heating in a Nonrotating Atmosphere without Friction

In a nonrotating atmosphere the effective Coriolis parameter f is zero, and this may be interpreted as the burning in a region along the rotational equator of an NS. Consider a part of the atmosphere of a large lateral extent with the two-layer fluid described above in the equilibrium configuration with, for example, $h_1 = h_2$ initially. The fluid is allowed to freely leave and enter the domain through the sides. For a δ-function heat source $Q = Q_0 \delta(x)$ and zero friction between the layers ($\mu_f = 0$) we can find a steady state solution that will be achieved after an initial transient. The solution will have a uniform divergent flow at the upper layer, satisfying $h_2 v_{2x} = Q_0[\Theta(x) - \frac{1}{2}]$, and a uniform convergent flow at the bottom layer, with $h_1 v_{1x}| = -\epsilon Q_0[\Theta(x) - \frac{1}{2}]$, where $\Theta(x)$ is a step function. The equilibrium value of h_2, after the transient flow traverses the domain of interest, is larger by $\sim Q_0/(gh)^{1/2}$ than the initial thickness of the upper layer, while layer 1 is contracted by a similar amount. The main property of this solution is that, even though the heat source is continually operating, the temperature (or thickness) of the layers does not change in time after the initial transient has died out. The heating drives opposing winds in both layers, and the heating energy goes into raising the fluid from the bottom to the top. For small heating rates, $Q_0/h \lesssim (gh)^{1/2}$, the shearing flow between the two layers is stable to Kelvin-Helmholtz instability as a result of buoyant stratification.

This solution is valid until the outflow has reached the end of the lateral extent of the atmosphere, at which point layer 2 will grow at the expense of depleting layer 1. Such lowering of layer 2, i.e., the presence of high-entropy fluid at a lower height, represents simple heating of the whole atmosphere that we eventually expect from a heat source. Therefore, in order to have the heat source continuously increase the temperature locally, as is required for a local thermonuclear runaway, one needs a way of containing the outflow

over some spatial length scale. In the absence of lateral boundaries, this feat is accomplished by rotation of the star, friction, or both.

3.3. Localized Heating in a Rotating Atmosphere
3.3.1. General Considerations

The main new feature introduced into the dynamics in a rotating atmosphere is that when friction is absent, all disturbances do not relax to a state of minimum potential energy, in contrast to a nonrotating atmosphere. Instead, disturbances tend to relax rapidly (in a time of the order of one rotation period) to a state of geostrophic balance, where all pressure gradients are balanced by the Coriolis force acting on fluid moving along the isobars. A famous example is known as the Rossby adjustment problem (Gill 1982): a uniformly rotating fluid of constant density is released with an initial step in its height distribution. A transient ensues, in which the fluid starts to spread. The spread is slowed down, however, by the action of the Coriolis force, and the fluid oscillates around the equilibrium configuration, radiating gravity waves. The end result is a state of equilibrium with nonzero kinetic energy in the flow such that the adjusted pressure gradient is balanced by the Coriolis force. A simple way of understanding the spatial scale on which the equilibration occurs is to consider the momentum equations for a single incompressible layer of constant depth H_0 with a perturbation $h = H_0 + \delta h$:

$$\frac{dv_x}{dt} = -g\frac{\partial}{\partial x}(H_0 + \delta h) + fv_y, \qquad (46)$$

$$\frac{dv_y}{dt} = -fv_x. \qquad (47)$$

Equation (47) can be integrated to give $v_y = f\Delta x$, i.e., the transverse velocity of the fluid element is proportional to the displacement from its initial position. Substituting this into equation (46) with the assumption of geostrophic balance and estimating the pressure gradient as $gH_0/\Delta x$, we obtain the characteristic length over which the pressure gradient is spread: $\Delta x = (gH_0)^{1/2}/f$. This is the Rossby radius of deformation for a rotating atmosphere of scale height H_0. After the transient, the initial step in height of the fluid will transform into a gradual slope over the length scale of Rossby radius.

The above argument is valid only if the horizontal displacement of the fluid element, Δx, is of the same order of magnitude as the length scale over which the pressure gradient is spread. This is true only for large initial perturbation, $\delta h \sim H_0$. However, the conclusion that the pressure gradient is spread over the Rossby radius turns out to be valid even if the initial perturbation is not large. For a small perturbation, the spread of the pressure gradient does not involve actual motion of a fluid element over Δx but is communicated via gravity waves. In the presence of rotation, the gravity waves are dispersive, with dispersion relation $\omega^2 = f^2 + c_g^2 k^2$, where $c_g = (gH_0)^{1/2}$. For wavelengths shorter than the Rossby radius, gravity waves are unaffected by rotation and leave the region of disturbance, while for wavelengths longer than c_g/f, the propagation speeds become very small. Only the long-wavelength component of the initial perturbation is left behind, and even for small initial perturbations the geostrophic balance is eventually established on the length scale of the Rossby radius,

$(gH_0)^{1/2}/f$. We refer the reader to Gill (1982) for further details.

3.3.2. Localized Heating in a Rotating Atmosphere without Friction

We now study the flows in a rotating atmosphere forced by a localized heat input. We concentrate on the top layer of the isentropic model discussed above. If we assume that the density contrast between the two layers is large enough ($\epsilon \ll 1$), then the height of level 1 does not change appreciably during the evolution. In that case, the linearized equations for the top layer of thickness $h = H_0 + \delta h$ become

$$\frac{\partial h}{\partial t} + H_0 \frac{\partial}{\partial x} v_x = Q(x, t) , \tag{48}$$

$$\frac{\partial v_x}{\partial t} = -g \frac{\partial}{\partial x} h + f v_y , \tag{49}$$

$$\frac{\partial v_y}{\partial t} = -f v_x . \tag{50}$$

We will further refer to models tracking only the top fluid layer as one-layer models. We find that they contain most of the essential physics of the two-layer system. If the timescale of heating is much slower than the time it takes gravity waves to propagate over the characteristic Rossby radius (i.e., $1/f$), at each moment in time the system will be in approximate geostrophic balance. We thus omit the time derivative in equation (49); this also automatically filters out transient gravity waves. The system of equations can now be combined to yield a single equation for the height of the layer:

$$h - a_R^2 \frac{\partial^2 h}{\partial x^2} = \int_0^t Q(x, t') dt' . \tag{51}$$

This is a forced Klein-Gordon equation, where the source term is provided by the total heating at a particular point. The Green's function for the left-hand side of the equation is $G(x\,|\,\zeta) = 1/2a_R\, e^{-|x-\zeta|/a_R}$. Therefore, for a constant δ-function heating $Q(x, t) = Q_0 \delta(x)$ the fluid follows a growing vortex sheet solution:

$$h(x, t) = \frac{Q_0 t}{2a_R} e^{-|x|/a_R} , \tag{52}$$

$$v_x(x, t) = \mathrm{sgn}\, x \frac{Q_0}{2H_0} e^{-|x|/a_R} , \tag{53}$$

$$v_y(x, t) = -\mathrm{sgn}\, x \frac{Q_0 t f}{2H_0} e^{-|x|/a_R} . \tag{54}$$

A few points should be made about this solution. It shows that, for constant heating, the height of the layer (or its temperature) grows linearly in time in a region of characteristic size equal to the Rossby radius around the heat source. Aside from nonlinear effects, the size of the area affected by heating does not change as the height increases. Therefore, the pressure gradient increases linearly with time. The velocity transverse to the pressure gradient (geostrophic velocity v_y) also grows linearly with time. If we were to solve the same problem with cylindrically symmetric localized heating, the geostrophic flow would create a vortex-like circulation around the source of heating. When $Q_0 > 0$, the heated region is the area of high pressure, and hence the

sense of geostrophic velocity in the layer is anticyclonic (opposite to the sense of rotation of the star), and cyclonic in a low-pressure region for the case of cooling. The discontinuity in velocity at $x = 0$ is an artifact of the δ-function forcing. Since realistic forcing is distributed over a finite area, the velocity should smoothly go to zero at the center of heating. Another feature of the solution is the presence of a nonzero flow away from the source of heating (and the opposite for cooling). This flow is not due to the pressure gradient as such, but rather due to a time rate of change in the pressure gradient as the central pressure rises or falls. Such a flow is known as the *isallobaric wind* (Holton 1992) and is not itself in geostrophic balance. However, this wind plays an important role in the adjustment to balance as can be seen from equation (50). In order for the geostrophic velocity to change in response to modified conditions, there must be a nonzero ageostrophic velocity (see eq. [18]). Since all quantities in the above solution exponentially decay at distances larger than the Rossby radius, the effects of heating are thus localized as a result of rotation.

3.3.3. Localized Heating in a Rotating Atmosphere with Strong Friction

When there is (turbulent) viscosity in the system, frictional forces need to be added to the right-hand side of equations (49) and (50):

$$\frac{\partial h}{\partial t} + H_0 \frac{\partial}{\partial x} v_x = Q(x, t) , \tag{55}$$

$$\frac{\partial v_x}{\partial t} = -g \frac{\partial}{\partial x} h + f v_y - \frac{v_x}{t_{fr}} , \tag{56}$$

$$\frac{\partial v_y}{\partial t} = -f v_x - \frac{v_y}{t_{fr}} . \tag{57}$$

Here $1/t_{fr}$ is the coefficient of frictional drag (see § 2.3). For $1/t_{fr}, f \gg 1/t_n$ we can neglect the time derivatives on the left-hand side of equations (56) and (57). We then get

$$\frac{\partial h}{\partial t} + D \frac{\partial^2 h}{\partial x^2} = Q(x, t) , \tag{58}$$

$$v_x = -\frac{D}{H_0} \frac{\partial h}{\partial x} , \tag{59}$$

$$v_y = -f t_{fr} v_x , \tag{60}$$

where

$$D = \frac{t_{fr} g H_0}{1 + (f t_{fr})^2} . \tag{61}$$

Equation (58) is a diffusion equation with the source term Q and the diffusion coefficient D. For a localized heating $Q(x, t) = Q_0 \delta(x)$ switched on at $t = 0$, the solution is given by

$$h(x, t) = Q_0 \sqrt{\frac{t}{4\pi D}} F\left(\frac{x}{2\sqrt{Dt}}\right) , \tag{62}$$

where

$$F(q) = q \int_q^\infty \frac{1}{q_1^2} e^{-q_1^2} dq_1 . \tag{63}$$

The height (i.e., temperature) and velocity perturbations are concentrated within the diffusion length $\delta x = (Dt)^{1/2}$.

3.3.4. Implications for Burst Ignition Length Scale

What can we learn from the atmospheric response to localized heating? We saw that for a frictionless rotating atmosphere, the temperature perturbation is confined to the Rossby adjustment radius, hence the ignition of the burst is likely to happen on that scale. When there is strong friction, the temperature perturbation is confined to the diffusion length scale. In this case, we therefore expect the ignition to happen on the scale $\delta x_{\mathrm{ignition}} \sim (D t_n)^{1/2}$, where D is the diffusion coefficient given by equation (61) and t_n is the characteristic nuclear burning timescale. As we saw in the previous section, and as will be confirmed by simulations in the next section, these ignition length scales are of the same order as front widths in respective cases (see eqs. [22] and [34]). The only difference is that in the case of the front propagation the important scale height is that of the hot part of the ocean, whereas for the ignition the scale height H_0 is that of the unheated, cold ocean.

3.4. Burning Front Propagation

When we numerically solve the system of equations (40)–(45) with a temperature-sensitive heating function, we find that a local runaway can develop into a propagating burning front solution. In order to simulate conditions relevant to the case of an NS atmosphere during a burst, we consider heating due to a 3α helium-burning reaction and one-zone cooling due to blackbody radiation (see, e.g., Cumming & Bildsten 2000):

$$Q = 5.3 \times 10^{21} \text{ ergs g}^{-1} \text{ s}^{-1} \frac{\rho_5^2 Y^3}{T_8^3} \exp\left(\frac{-44}{T_8}\right) - \frac{acT^4}{3\kappa y^2} .$$

(64)

Here ρ_5 is the density in units of 10^5 g cm^{-3} (which we evaluate including degenerate corrections), Y is the helium abundance obeying $dY/dt = \epsilon_{3\alpha}/(5.84 \times 10^{17} \text{ergs})$, T_8 is the temperature in units of 10^8 K, and κ is the opacity, which, for simplicity, we take to be a constant, 0.03 cm^2 g^{-1}. Hydrogen, if present in the NS envelope, will burn and release energy as well. However, for NSs in LMXBs considered here, accreting at $\dot{M} \gtrsim 2 \times 10^{-10} M_\odot$ yr^{-1}, the NS envelope is so hot ($T > 8 \times 10^7$ K) that hydrogen burns via the hot CNO cycle, whereby the rate-limiting steps are not proton captures but beta decays (see Bildsten 1998 for review). Under these conditions, the hydrogen-burning rate is independent of the temperature of the envelope and is thermally stable. It is the thermally unstable helium burning that is responsible for the runaway during the burst, which justifies using the 3α rate as the heating function. While being representative of the conditions in a type I burst, this function is by no means complete. In particular, we neglected the electron screening of the 3α reaction (Fushiki & Lamb 1987), as well as further energy release due to nuclear evolution beyond carbon. We find, however, that the physics of front propagation is independent of the details of a particular heating function as long as this function has a rise, has a single peak, and decays at high temperatures.

For our initial state we consider the atmosphere of pure helium with column depth $y = 5.4 \times 10^8$ g cm^{-2} at the point of ignition. The temperature at the start of the runaway (determined as the point where temperature derivatives of heating and cooling match) is $T_8 = 1.64$. The height of the top fluid layer, which in our model represents

temperature, is normalized in units of the scale height of the unperturbed atmosphere. In order to set off the runaway, we raise the temperature at one location on our grid on a scale much smaller than the Rossby radius. The sequence of snapshots of subsequent evolution of layer height (temperature), instantaneous net heating $Q(x, t)$, and ageostrophic and geostrophic velocities in the top layer is shown in Figure 4 in the one-layer limit of our model ($\epsilon = 0$).[6] In this simulation, the Coriolis parameter is constant everywhere on the grid and is representative of a star with 250 Hz rotation frequency at 45° latitude. First we discuss simulations for the case without interlayer friction ($\mu_f = 0$ in eqs. [40]–[45]).

The initial height perturbation introduces potential energy, about $\frac{2}{3}$ of which is radiated into gravity waves, and the rest ends up in a geostrophically balanced flow which is established within a rotation period and has a characteristic length scale of a Rossby radius. As expected, the initial stage of growth is similar to the δ-function response described above: the vortex intensifies while maintaining its width. Since in the beginning of the runaway the heating is a strongly increasing function of temperature, the dominant contribution to vortex intensification comes from the fastest growing central part. The heating function given by equation (64) goes through a peak during the runaway at about 9×10^8 K for our parameters before cooling catches up with heating at about 2×10^9 K. When the central temperature moves past the peak heating and the tails of the vortex start undergoing the fast part of the runaway, a double-peaked structure of the heating function appears as seen in Figure 4. As the heating peaks separate, the vortex begins to spread and the structure of a burning front appears: a localized area with the runaway heating which moves into the unburned material at a constant speed. The burning is accompanied by a rise in layer thickness, so that there is a substantial pressure gradient in the direction of motion of the front. In the absence of friction, this pressure gradient is closely balanced by the Coriolis force acting on the flow generated parallel to the front. As discussed in § 2, the unbalanced ageostrophic component is present and necessary to drive the change in the much larger geostrophic flow: $dv_{\mathrm{geostrophic}}/dt = -f v_{\mathrm{ageostrophic}}$. It is the ageostrophic flow (typically smaller in magnitude by a factor of order $1/f t_n \sim 2 \times 10^2$ compared to its geostrophic counterpart) which is responsible for the front propagation.

3.5. Structure and Speed of the Front

The temperature at a location ahead of the front increases as a result of two effects: influx of the ageostrophic wind of hot material across the front and local thermonuclear energy generation. The local heating rate due to thermonuclear reactions, which sensitively depends on the temperature, will start to grow if the temperature perturbation is sufficient to push the fluid parcel into the runaway regime. We are assuming that the temperature and column

---

[6] For our numerical method we use second-order accurate finite differencing of model equations. This allows us to cut down on numerical diffusion that can artificially increase front speeds. Since the underlying equations support fast-moving dispersive gravity waves, special attention is paid to boundary conditions. To allow for integration times longer than the gravity wave crossing time, we introduce an absorbing boundary layer (Romate 1992) that dissipates the gravity waves of wavelength smaller than the size of the boundary layer. To prevent reflection of longer wavelengths, we add the nonreflecting condition that eliminates backward-going characteristics at the boundary (Thompson 1987).
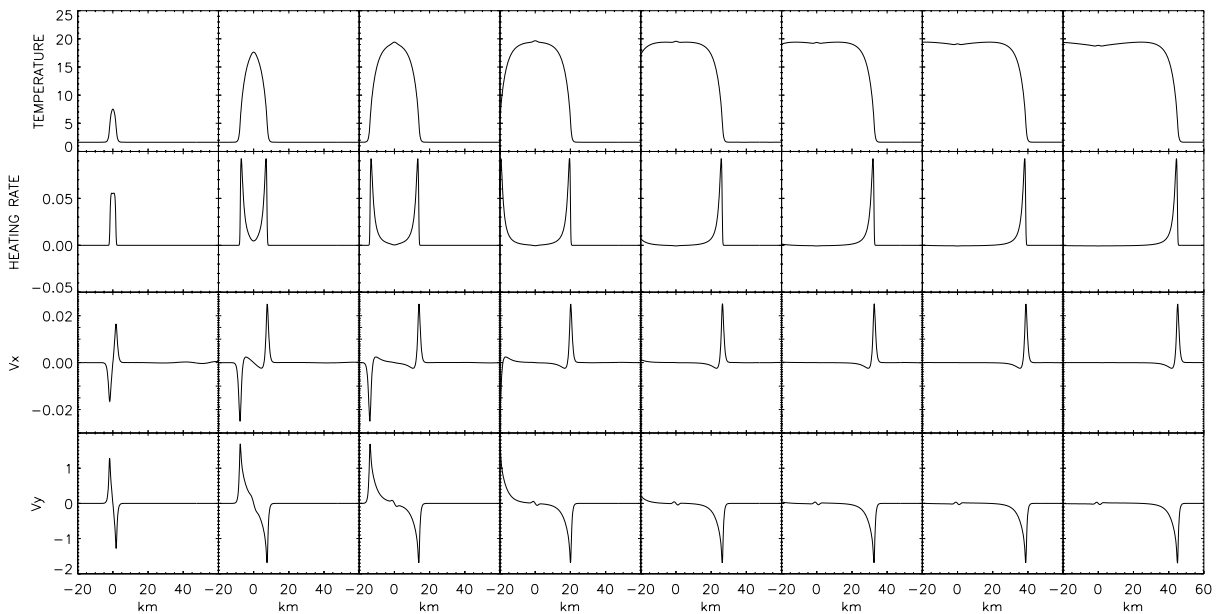
FIG. 4.—One-layer model of the evolution of a localized source of heating into two propagating burning fronts. Shown from top to bottom are the temperature (scale height) of the layer in units of 10^8 K, the instantaneous heating rate (in units of 5×10^{19} ergs g^{-1} s^{-1}), the cross-front ageostrophic velocity v_x, and the geostrophic velocity v_y parallel to the front (velocities are in units of gravity wave speed of the cold material, 1.5×10^8 cm s^{-1}). Time is increasing left to right with frames separated by 0.125 s.

depth in the fluid are such that by raising the temperature sufficiently the runaway will start. In this case, since the temperature well inside the burning front is high enough for a runaway, we are guaranteed that even if the fluid before the front is colder than the point of marginal stability, it will cross into the runaway as the front approaches. When the friction is absent, the fluid motion across the front is driven by the time rate of change in the pressure gradient: $v_x = -(g/f^2)(d/dt)\nabla h$ (see eq. [20]). As the front approaches, the pressure gradient increases in magnitude (it is negative for a front moving to the right) and reaches the maximum at the point of peak heating. The fluid is thus pushed through the front, igniting material ahead, and the pressure gradient is performing work to accelerate this fluid to the geostrophic velocity. The width of the front is thus set by the magnitude of the Coriolis force which turns the cross-front fluid motion into the flow parallel to the front. Since the scale height inside the front can change by factors of order 10 for strong bursts, nonlinear effects become important. Typically, however, the characteristic front thickness is of the order of the Rossby radius in the hot material behind the front (~ 3 km for our parameters; see eq. [24]). Since the burning must be complete inside the front width, the speed of the front should be such that it moves one Rossby radius in a characteristic nuclear time. For our parameters, it takes 0.1–0.2 s to go through the fast part of the 3α burning, which yields an estimate of 15–30 km s^{-1} for the front speed. Behind the location of peak heating the temperature continues to rise, but the magnitude of the pressure gradient starts to decrease, and the isallobaric wind is directed opposite to the motion of the front. The relative amount of cross-front fluid motion in the forward and backward directions can dramatically influence the speed of propagation of the front and depends on frictional effects due to (turbulent) viscosity and on drag due to momentum-conserving transport of fluid between layers. We shall refer to the latter effect as momentum coupling.

Figure 5 shows the internal structure of two fronts computed in the one-layer approximation with identical heating functions but differing in the strength of momentum coupling. Front A (Fig. 5a) is computed without the terms proportional to $(v_{2x,y} - v_{1x,y})$ in equations (40)–(45) (momentum-nonconserving front), while front B (Fig. 5b) is computed with momentum-coupling terms retained. Viscous friction is turned off in both cases ($\mu_f = 0$). Physically, case A represents the situation in which the fluid from the cold layer is being injected into the hot layer at the velocity of the hot layer, while in B the fluid is injected maintaining the velocity of the cold layer (which is zero for one-layer case $\epsilon \ll 1$). In the latter case, as the injected fluid is accelerated to the velocity of the hot layer, it exerts drag on the hot layer, which is reflected in the friction-like velocity dependence in the coupling terms in equations (40)–(45).[7]

The two fronts move with different speeds: front A achieves 20 km s^{-1}, while front B has a speed of 60 km s^{-1}. The main qualitative difference in the structure of these fronts is the variation of ageostrophic velocity v_x with position inside the front. For front A the cross-front displacement of a fluid element is symmetric, with a fluid particle returning to the same x-coordinate after the front passes, while for front B the ageostrophic component is asymmetric, skewed toward higher forward velocity. With stronger cross-front circulation front B achieves a larger speed of propagation. The cause of the larger ageostrophic velocity in case B is the modification of the geostrophic balance brought by the momentum-coupling drag. The isal-

---

[7] Such drag converts some energy from the flow in the hot layer into heat. According to our model, heating represents injection of fluid into the top layer, so, if one is to be precise, the heating function should be renormalized to account for the frictional heating. When included in simulations, however, such renormalization accounted for no more than a 25% increase in front speeds, while not affecting the qualitative picture. Henceforth we will ignore the frictional heating.
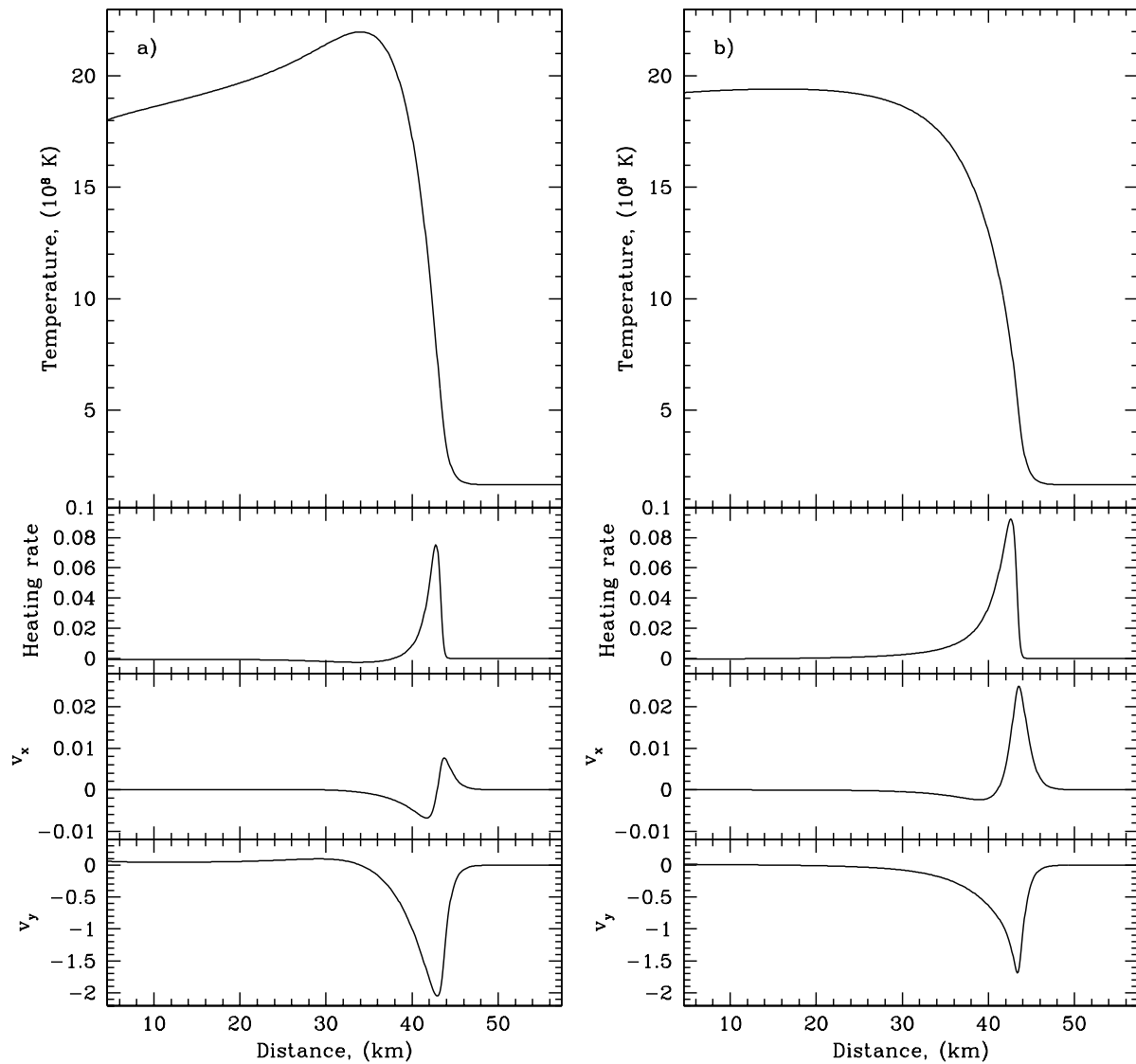
Fig. 5.—Internal structure of burning fronts in the one-layer model. Shown are the temperature of the layer, the instantaneous heating rate (in units of 5×10^{19} ergs g^{-1} s^{-1}), the cross-front ageostrophic velocity v_x, and the tangential geostrophic velocity v_y (velocities in units of gravity wave speed in the cold material, 1.5×10^8 cm s^{-1}). (a) Front without the drag due to momentum coupling. (b) Momentum-coupling drag included.

lobaric wind relationship is now $v_x = -(g/f^2)[(d/dt)\nabla h + (Q/h)\nabla h]$. Since $Q/h \sim 1/t_n$, the two terms in this formula are of the same order of magnitude, and the cross-front wind is enhanced where the magnitude of the pressure gradient is growing with time (ahead of the peak heating) and diminished where the pressure gradient is falling. As the heat transport depends on the cross-front circulation, the momentum-conserving front should exhibit larger speed of propagation. This is consistent with the results obtained in § 2, where it was shown that, in general, friction can increase the front speed.

The nature of the temperature overshoot in Figure 5a can also be attributed to the differences in ageostrophic velocities between the two fronts. In front A, the hot fluid flows toward the back of the front as much as it does in the forward direction. This flow increases the temperature of the fluid at the back of the front beyond the equilibrium value. After the helium fuel is depleted, the material cools by radiation, and a "cooling tail" develops because of the time delay in the start of cooling due to the finite speed of the front. Momentum-conserving fronts also develop cooling

tails, but because of the larger propagation speed, the front moves through a larger distance before the fuel depletes enough for cooling to dominate heating (see discussion in § 4.3).

We can derive a formal expression for the front propagation speed by transforming equations (40)–(45) for the one-layer model to the frame comoving with the front. Expressing the ageostrophic component v_x as a sum of constant front speed v_f and a residual v'_x, and assuming that in the comoving frame the front is not evolving in time, we obtain

$$\frac{\partial}{\partial x}(hv'_x) = Q , \tag{65}$$

$$v'_x \frac{\partial}{\partial x} v'_x = -g \frac{\partial}{\partial x} h + fv_y - \frac{Q + \mu_f}{h}(v'_x + v_f) , \tag{66}$$

$$v'_x \frac{\partial}{\partial x} v_y = -f(v'_x + v_f) - \frac{Q + \mu_f}{h} v_y . \tag{67}$$

As can be seen from Figure 5, the geostrophic velocity v_y reaches an extremum inside the front. Denote all values at this point with an asterisk. At the extremal point, $v'_x|_* = -v_f - v_y^*[Q(h^*) + \mu_f]/h^*$, and we can solve the above system of equations for the speed of the front:

$$v_f = -\left[\frac{Q(h^*) - h^*(\partial/\partial x)v_x|_*}{(\partial/\partial x)h|_*} + \frac{v_y^*}{f}\frac{Q(h^*) + \mu_f}{h^*}\right]. \quad (68)$$

Momentum-coupling and viscous friction effects are contained in the second term on the right-hand side of equation (68). Without them the speed of front propagation is controlled by the effective heating and the pressure gradient at the peak of the geostrophic velocity. The effective heating $Q(h^*) - h^*(\partial/\partial x)v_x|_*$ is the nuclear energy generation minus the heat carried by the cross-front flow. When the pressure gradient at the peak is approximated as h^*/a_R, we get that

the front speed is set by the characteristic front width divided by the effective burning time, as in equation (6). The momentum-coupling drag term is of the same order of magnitude as the first term in equation (68) and increases the speed of propagation and the width of the front by a factor of 2–3.

3.6. Multilayer Dynamics

Although illustrative, the one-layer model represents the motion of only the hot layer of fluid and does not capture all of the dynamics of the front. In order to better understand the propagation of the deflagration front through the NS atmosphere, we numerically solve the time-dependent system of equations (40)–(45) for two layers of isentropic fluid. Figure 6a demonstrates the structure of the developed momentum-conserving burning front without interlayer friction propagating from left to right. In this particular run the density contrast ϵ was set to 0.2, with the initial thick-
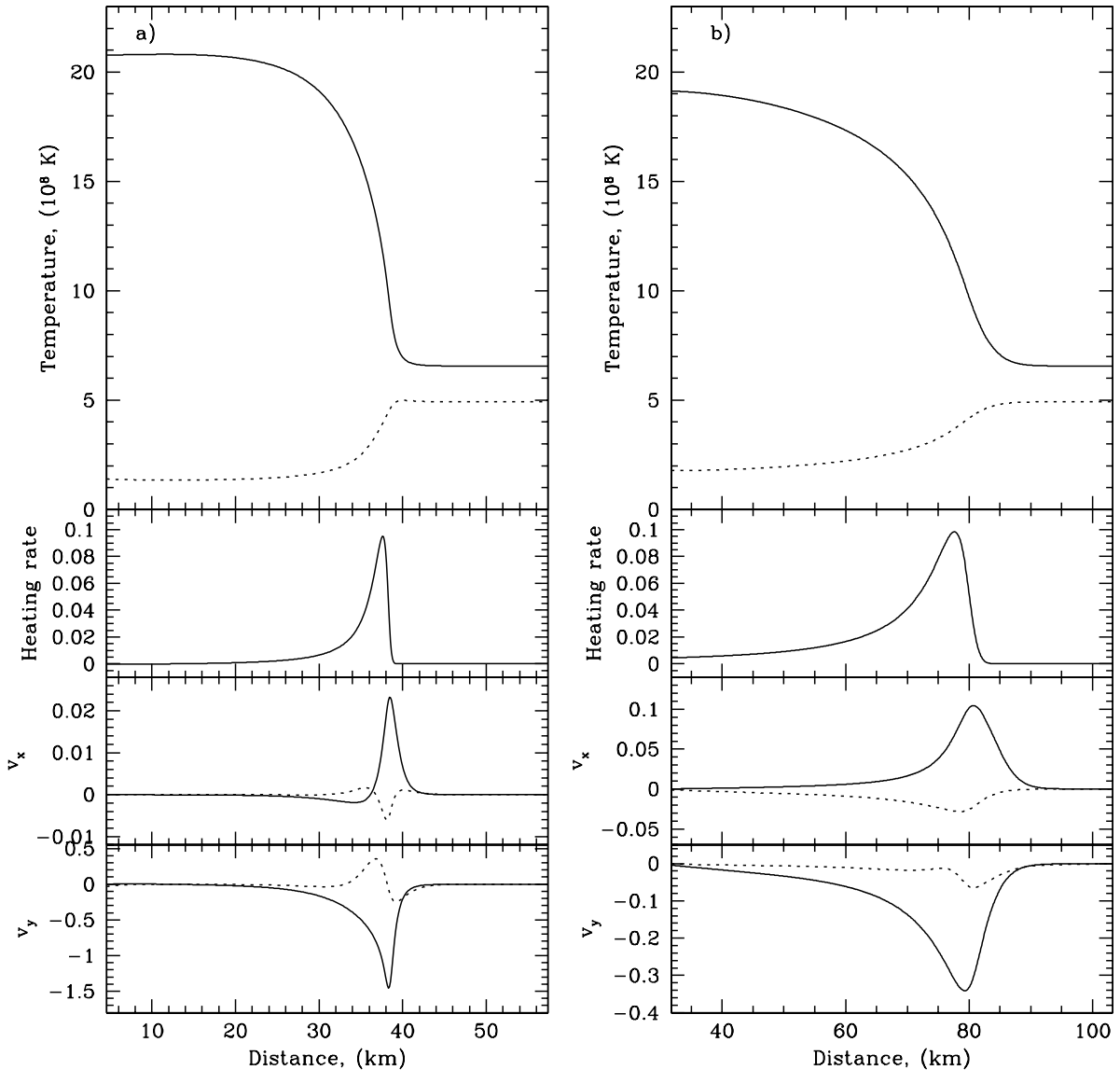

FIG. 6.—Internal structure of burning fronts in the two-layer model with $\epsilon = 0.2$. Shown are the thickness (temperature) of the layers with layer 2 (*solid lines*) added to layer 1 (*dashed lines*), the instantaneous heating rate (in units of 5×10^{19} ergs g^{-1} s^{-1}), the cross-front ageostrophic velocity v_x, and the tangential geostrophic velocity v_y for two layers (velocities are in units of gravity wave speed of the cold material 1.5×10^8 cm s^{-1}). (*a*) Momentum-conserving front without viscous friction ($\hat{\mu}_f = 0$). For demonstration purposes, v_x and v_y for the bottom layer are increased by factors of 2 and 5, respectively. (*b*) Momentum-conserving front with friction ($\hat{\mu}_f = 1$); v_y for the bottom layer is increased by factor of 5.

ness of the lower layer chosen to be 3 times the thickness of the top layer. The first panel shows the evolution of layer thickness through the front. As the fluid is pumped to a higher entropy state, layer 2 expands and layer 1 contracts; the ratio of contraction to expansion is proportional to the density contrast. We take the horizontal location of the peak in the heating rate as the center of the front. From the plot of the ageostrophic velocities we see that there is a divergence of the fluid at the top level and a convergence at the bottom level. The low-entropy fluid is drawn toward the center of the front and after ignition outflows in the high-entropy layer. The motion of fluid at the lower layer can also be interpreted as a response to the gradient in the column depth across the front created by divergence of the light fluid on top. In addition to creating convergence toward the center, the overpressure ahead of the front center also forces some flow to go in the direction of front motion. This "snowplow" effect will become important in the regime of strong top-bottom coupling (see the next subsection).

The dominant component of motion in both layers is the geostrophic velocity (third panel of Fig. 6a). The direction of this flow is different between the layers: divergence at the top generates anticyclonic motion, while convergence at the bottom generates cyclonic motion. The fluid velocity in the upper level is larger than that in the lower level. The relative velocities in the two layers depend on the density contrast and the interlayer friction.

3.7. Frictional Effects

We have argued in § 2 that friction between the top and the bottom of the atmosphere modifies the geostrophic balance within the front and changes the velocity of the flow across the front. The cross-front velocity attains properties of a diffusive flow governed by the diffusion constant given by equation (61). Of course, the diffusion analogy is only formal and refers to the spreading of pressure gradients with time in the presence of friction. Depending on the strength of frictional coupling, the speed of the front may be either enhanced or diminished (see eq. [35]). Recall that in our analytical estimates (§ 2) we parametrized the strength of friction by the coupling time t_{fr}, while in our two-layer model, described by equations (40)–(45), the friction strength is parameterized by μ_f/h, where μ_f is a constant. To facilitate the comparison between analytical and numerical results, we define, for our one-layer model, the characteristic timescale of frictional coupling as $t_{\text{fr}} = h^*/\mu_f$, where h^* is the layer height at the peak of the geostrophic velocity inside the front (in the presence of friction this is approximately but not exactly the location of peak heating). In Figure 2 we plot the speed of the front obtained from one-layer simulations versus the dimensionless friction parameter $\hat{\mu} \equiv (t_{\text{fr}} f)^{-1}$ and show the fit using the analytic formula for the front speed in equation (34).

There are several distinct regimes depending on how the timescale of frictional forcing compares to the characteristic timescales of the problem. When $1/f < t_n < t_{\text{fr}}$ (or $\hat{\mu} < 0.01$ for our parameters), the effects of friction are insignificant and the speed is close to the value obtained in § 3.5 after including momentum coupling (~ 60 km s^{-1}). For $1/f < t_{\text{fr}} < t_n$ ($0.01 < \hat{\mu} < 1$) the speed increases as $[\hat{\mu}/(1 + \hat{\mu}^2)]^{1/2}$ in agreement with equation (34). The friction in this regime acts to reduce the geostrophic velocity, which extends the front over a larger spatial scale. The cross-front diffusion

constant given by equation (61) is maximum when friction acts on the rotation timescale $\hat{\mu} = 1$, and at this value the front speed reaches the peak value (464 km s^{-1} for our parameters). The structure of the two-layer model at $\hat{\mu} = 1$ is shown in Figure 6b. The main distinction of this case from the case of zero friction (Fig. 6a) is the form and the larger magnitude of the ageostrophic speed, which implies very strong cross-front circulation. In the top layer the flow is purely in the forward direction with a strong return current in the bottom layer. The value of the geostrophic speed is clearly reduced compared to the no-friction case, and the strong coupling between the layers causes the flow on the bottom to have the same anticyclonic direction as the flow in the top layer.

When the friction is further increased ($\hat{\mu} > 1$), the cross-front diffusion (eq. [61]) diminishes and the front speed decreases. The cross-layer coupling now acts to reduce the ageostrophic component of velocity by making both layers move together. This "snowplow" effect eventually stalls the front when the friction is very large. Rather than create circulation across the front, the pressure gradient between the hot and cold material tries to push forward the whole cold atmosphere, which makes the front steepen and slow down.

It is interesting to speculate whether the extraordinarily high front speeds of hundreds of kilometers per second observed in simulations can be expected to occur in reality. One does not expect a well-defined burning front to arise if $t_{\text{prop}} < t_n$, where $t_{\text{prop}} \sim \pi R/v_{\text{front}}$ is the timescale on which the formed front would cross the half-circumference of the NS. In other words, it makes no sense to talk about a well-defined front with a width $\Delta \sim v_{\text{front}} t_n$ that is larger than the size of the star. This implies that if $v_{\text{front}} \gtrsim \pi R/t_n \sim 300$ km s^{-1}, the front never forms and the star is essentially ignited simultaneously. Depending on the physical source of friction in the NS atmosphere, there could then be two possible scenarios for the spread of nuclear burning. If the strong friction is temperature dependent and increases when the local perturbation grows into runaway (as may be the case for convective friction), the runaway will begin with no friction present and, therefore, will be confined to a hot spot of the size of the Rossby radius. As the runaway progresses, the friction will increase and the temperature perturbation will quickly (~ 0.1 s) spread over the NS surface. If, however, the friction is strong and present all of the time during the runaway (e.g., if a magnetic field is threading the fuel), an initial hot spot may not appear at all. Rather, the temperature perturbation spreads away from the heat source faster than the local thermonuclear runaway can develop, and the whole surface is likely to ignite almost simultaneously in a spherically symmetric fashion.

4. GLOBAL HYDRODYNAMICAL FLOWS DURING X-RAY BURSTS AND CONNECTION TO OBSERVATIONS

4.1. Likely Location of Burst Ignition

So far we have assumed that the preburst conditions are identical everywhere on the NS. However, because the star rotates, the effective gravity felt by the fluid elements near the equator is somewhat (up to $\sim 25\%$) smaller than that felt by the fluid elements near the poles. As we now argue, this asymmetry implies that, even if accretion is perfectly spherically symmetric, the fuel near the equator is likely to reach ignition conditions first.

We assume that, prior to a burst, the accreted material is brought into corotation with the rest of the star either by effective hydrodynamic viscosity produced by Rayleigh-Taylor or baroclinic instability (Fujimoto 1988), by weak hydromagnetic stresses, or even by microscopic viscosity (Cumming & Bildsten 2000). The timescales for the first two processes are small compared to the interval between the bursts, so this assumption is probably accurate as a zeroth-order approximation. We also assume that the gas deposited onto the star can redistribute to achieve hydrostatic balance,[8] and, as argued in § 1, we assume that magnetic fields, if present on the surface, do not create a permanent asymmetry by channeling the accretion flow.

In hydrostatic equilibrium, the pressure at the bottom of the accreted ocean should be the same everywhere,

$$p_{\text{bottom}} = m(\lambda)g_{\text{eff}}(\lambda) = \text{const} , \tag{69}$$

where $m(\lambda)$ is the accreted column density, $\lambda \equiv \pi/2 - \theta$ is the latitude, and $g_{\text{eff}} = |\nabla \phi|$ is the effective gravitational acceleration. Here ϕ is the sum of the gravitational potential, ϕ_{gr}, and the centrifugal potential, $\Omega^2 R^2 \cos^2 \lambda/2$. The effective gravity g_{eff} on the equator is less than that on the poles as a result of rotation of the star: $\delta g_{\text{eff}}/g_{\text{eff}} \sim (\Omega/\omega_K)^2$, where ω_K is the Keplerian angular frequency at the NS surface. For an NS rotating at 300–600 Hz, the relative difference is a few percent (up to $\frac{1}{4}$). Therefore, the column depth $m(\lambda)$ to a surface of a given pressure is a factor of $\delta g_{\text{eff}}/g_{\text{eff}}$ higher on the equator than on the poles. Now concentrate on two fluid elements, both at a pressure p_{bottom}, one of which is located on the equator while the other one is somewhere at a latitude $\lambda \neq 0$. Imagine that an additional amount of gas is accreted and is allowed to come to corotation and redistribute itself on the surface of the star in order to achieve hydrostatic balance. Our fluid elements will now be compressed to a pressure $p_{\text{bottom}} + \Delta p$ (since they are assumed to be in hydrostatic balance, they must have the same pressure). However, as is evident from equation (69), the increase in the column depth, $\Delta m(\lambda)$, must be larger on the equator than away from it. Therefore, fuel arriving on the equator will reach a given column depth faster than the fuel located off-equator. In other words, the local accretion rate is inversely proportional to the local effective gravity strength,

$$\dot{m}(\lambda) = \dot{m}_0 \frac{g_0}{g_{\text{eff}}(\lambda)} , \tag{70}$$

where $\dot{m}_0 = \dot{M}/(4\pi R^2)$ is the average local accretion rate and g_0 is the average acceleration of gravity, chosen so that the integral over the surface of the star $\int_{-\pi/2}^{\pi/2} \frac{1}{2} \cos \lambda [g_0/g(\lambda)] d\lambda = 1$. The local effective accretion rate seen on the equator is at least a few percent higher than that seen at the poles.

At a given local accretion rate, which determines the thermal profile of the accreted ocean, a certain critical column depth is necessary for the thermal instability and a thermonuclear runaway (see Bildsten 1998 for a review of spherically symmetric ignition conditions). As we argued above, the critical column depth necessary for a runaway will be achieved first close to the equator. We can therefore expect that ignition happens close to the rotational equator.

4.2. Burning Front Propagation on a β-Plane

The speed of the front propagation is larger near the equator,[9] where $f \rightarrow 0$, than near the poles, where $f \rightarrow f_{\text{max}} = 2\Omega$ (see eqs. [24] and [34]). To understand qualitatively the effect of the latitude dependence of the Coriolis parameter, we model front propagation on an x-y plane oriented with x-axis east and y-axis north. The Coriolis parameter is taken to be $f = \beta y$, where $\beta = 2\Omega/R$. This approximates a rotating sphere in the equatorial region and is known in geophysical literature as the equatorial β-plane.

4.2.1. One-Dimensional Simulations of Equatorial Ignition

We begin in one dimension with the simulation axis oriented along the y-axis from the equator to the north pole (and allow variation in quantities only along this direction). We solve a one-layer shallow water model without friction, which is initialized by increasing the temperature on the equator. A series of snapshots in time is shown in Figure 7. Since the Coriolis parameter is zero on the equator, it is not possible to establish geostrophic balance there. Gravity waves from the initial perturbation then propagate toward the pole until they are reflected from the region with a finite Coriolis parameter at approximately $y = a_{\text{RE}} \equiv [(gh)^{1/2}/\beta]^{1/2}$. This distance is called the equatorial Rossby radius and is the characteristic width of the equatorial waveguide for gravity waves. The trapped gravity waves are amplified by thermonuclear energy release on each pass. For our choice of initial conditions, after about $t_n(gh)^{1/2}/a_{\text{RE}} = t_n[\beta(gh)^{1/2}]^{1/2} \sim 10^2$–$10^3$ passes the whole equatorial waveguide region undergoes a runaway and two geostrophically supported burning fronts propagate toward the poles as "walls of fire." The propagating fronts steepen and slow down as expected because of the increasing f. For burning on a rotating NS the width and speed of the front

---

[8] Inogamov & Sunyaev (1999) have considered the spreading of material accreted onto a rotating NS from a thin equatorial disk. They have concentrated on the hot radiation pressure–dominated fluid at the very top of the atmosphere, which has not had time to frictionally couple to the rest of the star. The nuclear fuel participating in an X-ray burst is below the hot radiating layer considered by Inogamov & Sunyaev (1999). We therefore expect that the midlatitude "rings of fire" found by Inogamov & Sunyaev (1999) will not affect the location of burst ignition.

[9] Our equations break down at the equator because the horizontal Coriolis force due to vertical motion, $2\Omega \cos \lambda v_z \approx 2\Omega \cos \lambda(h/t_n)$, is no longer negligible compared to the Coriolis force due to horizontal motion, $fv_g \approx 2\Omega \sin \lambda(gh)^{1/2}$. However, this breakdown occurs only for latitudes $\lambda \lesssim (h/g)^{1/2}(1/t_n) \sim 10^{-5}$ (for typical values of h and t_n), i.e., very near the equator.
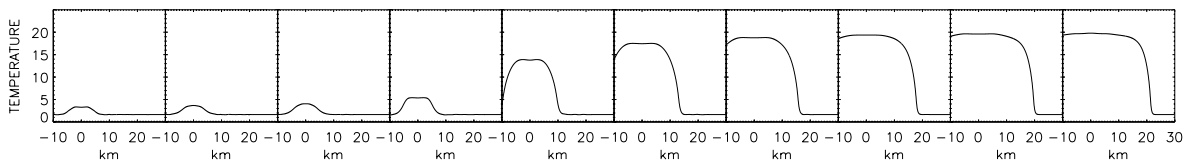
FIG. 7.—Ignition and propagation on β-plane. Frames are separated by 0.06 s.

decrease by a factor of $2\Omega/[\beta(gh)^{1/2}]^{1/2} \approx 4$ as the front propagates from the equator to the pole.

4.2.2. Two-Dimensional Model for Front Propagation

From equation (34) we can infer the front speed on the β-plane:

$$v_{\text{flame}}(\tilde{x}, \tilde{y}) = v_{\text{eq}} \frac{1}{\sqrt{1 + \tilde{y}^2}}, \qquad (71)$$

where $\tilde{x} = (\beta t_{\text{fr}})x$, $\tilde{y} = ft_{\text{fr}} = (\beta t_{\text{fr}})y$, and v_{eq} is the speed of the front at the equator. We have assumed for simplicity that $t_{\text{fr}} \ll t_n$; if this is not the case, then in the above expressions t_{fr} must be replaced by $t_{\text{fr}} t_n/(t_n + \eta t_{\text{fr}})$.

As was discussed in § 3.3, ignition happens over a patch of a finite size which is determined by the Coriolis parameter and the strength of friction in the atmosphere. However, for the current discussion, we assume that ignition is highly localized near some point on the β-plane. In Figure 8 we show how the front line develops depending on the location of the ignition point, $y_0 = f_0 t_{\text{fr}}$, where f_0 is the Coriolis parameter at the ignition location. To compute the evolution of the front line, we used the Fast Marching Method on a triangulated mesh (Sethian & Vladimirsky 2000) with speed function given by equation (71).[10] Below, we comment separately on the case in which the ignition point is on the equator and the case in which the atmosphere is ignited at some nonzero latitude.

4.2.3. Equatorial Ignition (Fig. 8a)

The front is roughly a circle until it reaches $|\tilde{y}| \simeq 1$, i.e., until it reaches the latitude where $f \approx 1/t_{\text{fr}}$ and the front speed is significantly reduced. Burning then quickly spreads along the equator, and the front line is nearly parallel to the equator when the flame reaches $\tilde{y} = ft_{\text{fr}} \sim 6$. For a typical strongly accreting NS in an LMXB the Coriolis parameter at the pole is 4–7×10^3 rad s^{-1}, and the typical frictional coupling strength $1/t_{\text{fr}}$ is anywhere between 10 s^{-1} for pure momentum coupling and 10^3 s^{-1} for frictional coupling by strong convective turbulence. Our simple two-dimensional

model then indicates that the front becomes parallel to the equator as soon as it reaches the midlatitudes, or perhaps even closer to the equator.[11]

What is the observational significance of this result? The asymmetry between north-south and east-west front propagation speeds and the dependence of the speed on the convective coupling strength may explain why only a fraction of X-ray bursts show detectable nearly coherent oscillations *during the burst rise*. Indeed, during the burst rise, while the flame, ignited at a spot, is still spreading around the star, rotational modulation of the X-ray flux should be evident. Yet it is observed only in some bursts. A possible explanation previously proposed in the literature (Miller 2000 and references therein) is that the oscillations in the X-ray flux are washed out when the burst X-rays scatter off a hot cloud which is thought to surround strongly accreting NSs. This explanation, however, does not resolve why there are oscillations in some bursts and no oscillations in others. Muno et al. (2001) recently concluded that, in fast (~ 600 Hz) rotators (as inferred from the burst oscillation frequency[12]), only the strong radius expansion bursts show oscillations during the rise, whereas for slower rotators (~ 300 Hz) there is no such correlation.

In our model, the equatorial front speed is larger than that at the poles, and, as argued in § 4.1, the burst is likely to ignite at the equator. If the disparity between the front speed at the equator and the poles is large (i.e., if $2\Omega t_{\text{fr}} \gg 1$), then the entire equatorial belt is likely to ignite in the beginning of the burst, and the asymmetry in burning which is needed for burst oscillations may disappear. Increasing the burst strength enhances the frictional coupling (makes t_{fr} shorter) and makes the burning pattern more asymmetric, thus making the burst oscillations during the rise more likely. This means that equatorially ignited strong bursts are more likely to be asymmetric than weak bursts. What about the dichotomy between fast (600 Hz) and "slow" (300

---

[10] We thank Alexander Vladimirsky for introducing us to this powerful method and helping to produce Fig. 8.

[11] When the front is parallel to the equator, the flows associated with the front are also parallel to the equator; such flows are referred to as zonal currents in geophysical literature. In this paper we do not consider in detail the nonaxisymmetric instabilities which may be present when the strength of the zonal current is latitude dependent, but see § 4.4.

[12] For one of the bursters, there is evidence that it spins at half of the burst oscillation frequency (Miller 1999; see also Strohmayer 2001).
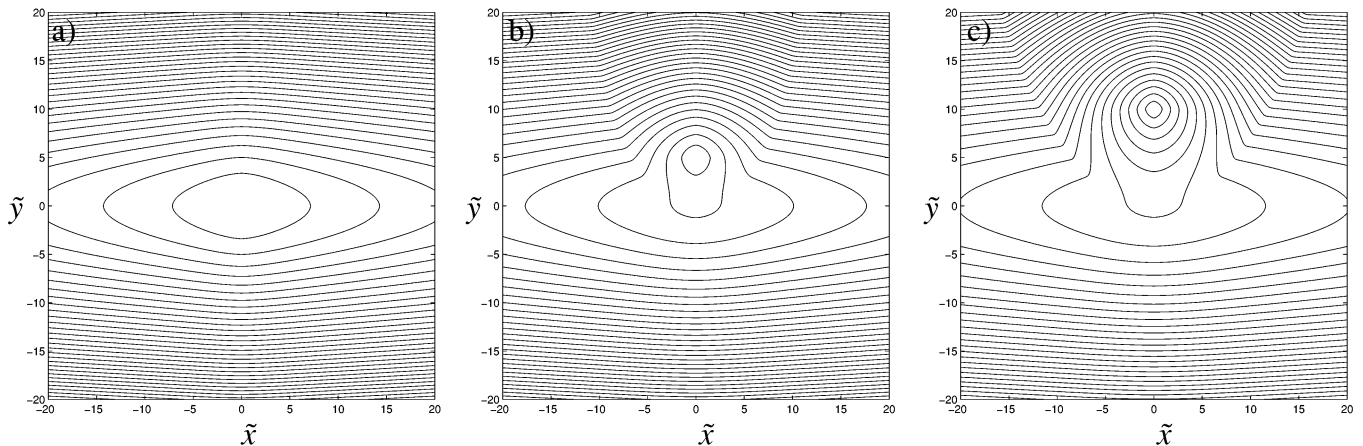

FIG. 8.—Two-dimensional propagation of burning front on β-plane for different ignition locations. Contour lines reflect front position at equal time intervals. (a) Equatorial ignition. (b) and (c) Ignition at higher latitudes. The dimensionless coordinates $\tilde{x}$ and $\tilde{y}$ are defined in § 4.2.

Hz) rotators? For slow rotators, the reduction in equatorial gravity due to rotation, discussed in § 4.1, is a factor of 4 smaller, so there may be a significant probability that bursts ignite off the equator and, hence, are more asymmetric regardless of burst strength.

4.2.4. *Nonequatorial Ignition* (*Figs. 8b and 8c*)

Ignition at higher latitudes can happen as a result of a variety of causes such as the variation in relative fraction of unburnt fuel over the surface that may depend on the history of previous bursts or peculiarities of the accretion flow (e.g., magnetic channeling). After nonequatorial ignition the front is roughly a circle so long as the distance to the ignition point $(\Delta \tilde{x}^2 + \Delta \tilde{y}^2)^{1/2}$ is less than 1. Beyond this distance, the front becomes increasingly deformed. As the edge of the flame approaches the equator, the front accelerates, and the equatorial belt is quickly ignited. After this, the evolution is similar to the equatorial ignition case discussed above.

4.3. *Zonal Flows and Frequency Drifts*

A salient feature of burst oscillations is their presence in the tails of bursts, presumably after the entire ocean has been burned, as well as the increase of the oscillation frequency as the star cools. We speculate on the possible *origin* of the inhomogeneity in the ashes that gives rise to the oscillations in § 4.4; here we discuss the implications of our global X-ray burst scenario on the *frequency* of these oscillations. In addition, we predict that yet unidentified oscillations may be present during the burst rise as well.

The burning front leaves hot ashes in its wake. These hot ashes then cool on a characteristic timescale t_{cool}, defined as $dh_{hot}/dt \sim h_{hot}/t_{cool}$. If burning starts in the equatorial region, as we have argued, then the equator has a head start in cooling, and in the cooling wake the equatorial temperature will be the lowest, increasing toward the poles. This temperature gradient will drive a zonal thermal wind directed backward relative to the NS rotation. If an inhomogeneous feature (e.g., a vortex; see the next subsection) is trapped in this backward zonal flow, the frequency of the flux modulation due to this feature will appear lower than the NS spin frequency. The speed of the backward flow can be estimated as follows:

$$v_{flow} \sim \frac{g}{f} \frac{\partial h}{\partial x} \sim \frac{g}{f} \frac{h_{hot}}{t_{cool} \, v_{flame}} . \tag{72}$$

The drift frequency corresponding to the flow is given by

$$\omega_{drift} = \frac{v_{flow}}{R \sin \theta} \sim \frac{\omega_K^2}{\Omega \sin (2\theta)} \frac{h_{hot}}{t_{cool} \, v_{flame}} . \tag{73}$$

In the midlatitude $v_{flame} \sim R/t_{rise}$, where t_{rise} is the timescale of the burst rise. The angular speed of the drift in the midlatitude is then

$$\frac{\omega_{drift}}{\Omega} \sim \left(\frac{\omega_K}{\Omega}\right)^2 \frac{t_{rise}}{t_{cool}} \frac{h_{hot}}{R}$$
$$= 3.6 \frac{h_{hot}}{R} \left(\frac{v_K}{2 \text{ kHz}}\right)^2 \left(\frac{300 \text{ Hz}}{v_s}\right)^2 \left(\frac{t_{rise}}{1 \text{s}}\right) \left(\frac{10 \text{s}}{t_{cool}}\right) . \tag{74}$$

Here v_K and v_s are surface Keplerian and spin frequency, respectively. For comparison, the frequency due to the radial expansion of the burning layer (Strohmayer et al.

1998; Cumming & Bildsten 2000) is

$$\left(\frac{\omega_{drift}}{\Omega}\right)_{lift-up} \sim \frac{h_{hot}}{R} . \tag{75}$$

The geostrophic drift from equation (75) and the lift-up drift from equation (75) are independent of each other, since the lift-up drift is related to the *horizontal* component of the spin vector which we have neglected in our calculations. Both drifts must be present in real bursts. One effect is not obviously dominant over the other; the "free" parameters in equation (75) decide which effect is more important for a particular burst.

Recently van Straaten et al. (2001), Galloway et al. (2001), Wijnands et al. (2001), and Cumming et al. (2002) showed that the lift-up drift is insufficient to explain the observed magnitude of the frequency drifts in some bursts. Perhaps the geostrophic wind could provide the missing piece. A significant amount of modeling of burst light curves is required to make a more detailed comparison with observations; this is the subject of our current research.

Note that from equation (73) one can infer significantly larger drifts close to the pole and the equator than the midlatitude drifts given by equation (75). However, close to the equator the geostrophic balance is broken, and equation (73) is no longer valid. The origin of divergence of ω_{drift} at the pole is that we formally take the distance to the pole to zero, while keeping nonzero v_{flow}. Perhaps, physically one should not consider distances to the pole closer than the width of the burning front.

Like the lift-up drift, the geostrophic drift velocity asymptotes to zero as cooling continues, since the scale heights at the equator and the pole equalize. Thus, the final X-ray modulation frequency asymptotes to the NS spin. A possible observational signature that can distinguish the two effects is the time dependence of the drift frequency. Consider an atmosphere undergoing blackbody cooling in the tail of the burst. The scale height of the atmosphere then decreases with time as $h(t) = h_{hot}(1 + t/t_c)^{-1/3}$, where $t_c = c_p \kappa y^2/(3acT_0^3)$ is the characteristic cooling time at the maximum expansion when the temperature is T_0. For $T_0 = 10^9$ K, $y = 5.4 \times 10^8$ g cm^{-2}, and $\kappa = 0.03$ cm^2 g^{-1}, this cooling time is 2 s. Since the geostrophic speed depends on the gradient of the scale height, the X-ray oscillation frequency due to geostrophic drift should change with time as

$$\frac{\omega(t)}{\Omega} = 1 - \frac{\omega_{drift}^0}{\Omega} \frac{1}{(1 + t/t_c)^{4/3}} , \tag{76}$$

where ω_{drift}^0 is the drift frequency at the start of cooling. Here we assumed that the feature that gives rise to the X-ray oscillations remains at the same latitude for the entire duration of the cooling tail of the burst and is carried by the geostrophic flow (however, see § 4.4 regarding the possibility of latitudinal drifts which can modify eq. [76]).

On the other hand, the frequency drift due to the radial expansion of the atmosphere depends on the scale height of the column, rather than its gradient. The oscillation frequency asymptotes to the NS rotation frequency as $1 - (\omega_{lift-up}^0/\Omega)(1 + t/t_c)^{-1/3}$. Since it is likely that in real bursts both the lift-up and the geostrophic drifts are present, the X-ray oscillation signal will have a time dependence corresponding to a superposition of the two effects. If both drifts are of the same order of magnitude, different time dependence of the two effects will result in the initial stage

of the frequency evolution being dominated by the geostrophic drift, while the late stage will be dominated by the lift-up drift. We note that the time scalings given above assume a very simplistic model of the evolution of the atmospheric scale height during the cooling. Clearly, more detailed simulations are necessary for robust comparisons with observations.

As demonstrated in §§ 2 and 3, the dominant flow during the burst *rise* is a geostrophic current directed parallel to the front line. For the moment, let us assume that the friction within the front is weak. Then the geostrophic current is given by $v_g \sim (gh_{\mathrm{hot}})^{1/2} \sim 1.5$–$3 \times 10^8$ cm s^{-1} and is independent of latitude (this follows from eqs. [19] and [24]). If there is a temperature inhomogeneity entrained in this current (similar to the inhomogeneities responsible for oscillations in cooling tails of bursts which were discussed above), we may expect a flux modulation at a frequency higher than the spin frequency; it will appear as an upper sideband of the main burst oscillation frequency during the rise. When the front is at a latitude λ, the frequency of this sideband is $v_g/(2\pi R \cos \lambda)$. As the flame propagates toward higher latitudes and carries the inhomogeneity along, the frequency chirps up.

The time evolution of this chirp is easy to estimate. The speed of the front depends on latitude as $v_f = v_f^{\mathrm{pole}}/\sin \lambda$, where $v_f^{\mathrm{pole}} \sim (gh_{\mathrm{hot}})^{1/2}/(2\Omega t_n)$ is the speed of the front near the pole. Expressing the front speed as $v_f = R \, d\lambda/dt$, we solve this equation for the front latitude as a function of time: $\cos \lambda = 1 - t/t_p$, where $t_p = R/v_f^{\mathrm{pole}}$. The time evolution of the sideband frequency is then

$$v_{\mathrm{chirp}} = \frac{v_g}{2\pi R \cos \lambda} = \frac{v_{\mathrm{chirp}}^{\mathrm{eq}}}{1 - t/t_p} . \qquad (77)$$

Here $v_{\mathrm{chirp}}^{\mathrm{eq}} = (gh)^{1/2}/2\pi R$ is the sideband frequency in the region of equatorial belt, which, for typical parameters in our simulations, ranges from 25 to 50 Hz. The final frequency of the chirp depends on how close to the pole the front stops propagating. If we take this halting distance to be one Rossby radius $a_R^{\mathrm{pole}} \sim 1$ km, the final frequency of the chirp is 10 times the equatorial value, or 250–500 Hz.

When friction is present, the speed of the zonal flow within the front is

$$v_{\mathrm{geostrophic}} \sim \frac{gh_{\mathrm{hot}}}{f\Delta} \sim \frac{gh_{\mathrm{hot}}}{ft_n v_{\mathrm{flame}}} , \qquad (78)$$

where v_{flame} is given by equation (34). We have then

$$v_{\mathrm{geostrophic}} \sim \left(\frac{gh_{\mathrm{hot}}}{t_n/t_{\mathrm{fr}}}\right)^{1/2} \frac{(f^2 + 1/t_{\mathrm{fr}}^2)^{1/2}}{f} . \qquad (79)$$

Close to the equator, where the Coriolis parameter f is small compared to the rate of frictional coupling $1/t_{\mathrm{fr}}$, the chirp frequency decreases as the front moves away from the equator. However, as soon as the front reaches the region with $f \sim 1/t_{\mathrm{fr}}$, the chirp frequency increases as the front moves farther toward the pole. When f is comparable to or greater than $1/t_{\mathrm{fr}}$, the magnitude of the chirp frequency is smaller by a factor of $\sim (t_n/t_{\mathrm{fr}})^{1/2}$ than what it would be if the friction was absent. If measured, the time dependence and the magnitude of the chirp frequency could be used to discern the importance of the effective viscosity during the burst.

4.4. *Vortices and Oscillations in the Tail*

So far we have not addressed the nature of the perturbations that lead to the oscillations in the X-ray flux in the burst tail. The speed of the cooling flow described in the previous subsection is latitude dependent (see eq. [72]). Thus, we can expect a strong zonal shear, of the type that is observed in the atmospheres of giant planets. Such a zonal shear is known to be unstable to formation of vortices; sometimes, like in the case of Jupiter, these vortices become large and occupy a significant fraction of the atmospheric surface. We speculate that these vortices do form in a cooling wake of an X-ray burst and are responsible for modulation of the X-ray flux in a burst tail. Currently we are constructing a two-dimensional shallow water simulation to address this scenario. Two-dimensional simulations will also allow us to study several other important effects which are not contained in the one-dimensional model. In particular, in the presence of a meridionally varying Coriolis parameter, vortices tend to acquire a drift even if there is no background flow. This effect is known as "β-drift" in the geophysical literature (see, e.g., Chan & Williams 1987) and is responsible for the northwest drift of tropical hurricanes on the Earth. The direction of the drift depends on the sense of rotation of the vortex, with cyclones drifting northwest and anticyclones southwest. In order to estimate the velocity of this drift, we use the empirical formula from Smith, Li, & Wang (1997): $v_{\beta\text{-drift}} \sim r_m(v_m \beta)^{1/2}$, where r_m is the radius where the maximum fluid velocity v_m relative to the vortex guiding center is reached. For a "hot spot" (anticyclonic) vortex with a radius equal to the Rossby radius (~ 1 km) and maximum internal speed $v_m \sim 10^8$ cm s^{-1} on a star with $\beta = 4 \times 10^{-3}$ cm^{-1} s^{-1}, the drift speed is of order 600 km s^{-1}. Depending on the direction of drift on the surface of the star, this effect can yield an X-ray oscillation frequency of up to 10 Hz lower than the spin frequency of the star. It remains to be seen how burning inside the vortex and potential nonaxisymmetric instabilities (e.g., development of spiral arms) modify this estimate and affect the evolution of vortices in two dimensions.

4.5. *MHD Dynamo and Coherence of Pulsations*

The burning front may be an ideal environment for an MHD dynamo:[13] it is likely to have both turbulence and, at least initially, strong shear; additionally, the typical eddy overturn time is much less than t_n. The equipartition value of the magnetic field is

$$B_{\mathrm{eq}} \sim 1\sqrt{4\pi\rho}v_c$$

$$\simeq 3 \times 10^9 \left(\frac{\rho}{10^6 \ \mathrm{g \ cm^{-3}}}\right)^{1/2} \left(\frac{v_c}{10^6 \ \mathrm{cm \ s^{-1}}}\right) \mathrm{G} , \qquad (80)$$

where, for concreteness, we have assumed that the turbulence is of convective origin. The coherence length of the dynamo-generated magnetic field is of the same order of magnitude as the ocean scale height.

As discussed in § 1, oscillations observed in the tails of X-ray bursts are highly coherent, with Q-values of a few thousand over the duration of the burst (van der Klis 2000).

---

[13] We thank Maxim Lyutikov for alerting us to this fact.

Both lift-up (Strohmayer et al. 1998; Cumming & Bildsten 2000) and geostrophic models for the drift have difficulty accounting for this coherence: the burning ocean is strongly sheared, with the top of the scale height moving at a different speed than the bottom. Cumming & Bildsten (2000) argued that convection might enforce the vertically rigid rotation of the burning ocean, although they pointed out that this is far from certain since convective turnover time is comparable to the spin period. Numerical models of bursts indicate that strong convection is indeed present when the ocean is ignited and rises but dies quickly when the fuel is exhausted and cooling begins. It therefore seems unlikely that the coherence of burst oscillations in the cooling tail of the burst could be accounted for by convectively enforced vertically rigid rotation.

We propose a different idea. The B field generated by the burning front will dynamically couple the top and the bottom of the cooling ocean[14] on the timescale (see, e.g., § 4 of Cumming & Bildsten 2000)

$$
\begin{aligned}
t_{\text{couple}} &\sim \frac{4\pi\rho h v_{\text{flow}}}{B^2} \sim \frac{h v_{\text{flow}}}{v_c^2} \\
&= 0.01 \text{ s} \left(\frac{h}{10^3 \text{ cm}}\right)\left(\frac{v_{\text{flow}}}{3 \times 10^7 \text{ cm s}^{-1}}\right) \\
&\quad \times \left(\frac{10^6 \text{ cm s}^{-1}}{v_c}\right)^2 ,
\end{aligned}
\tag{81}
$$

which is typically much shorter than the duration of the oscillations. Moreover, the coherence of the oscillations, $Q \sim t_{\text{cool}}/t_{\text{couple}}$, is of the order of magnitude of observed values. We therefore argue that the vertically rigid rotation necessary for the burst coherence may be enforced by the small-scale magnetic field generated by the dynamo in the burning front sweeping through the ocean during the burst rise. Note that after the burst this small-scale magnetic field is confined to the new ashes, while the freshly accreted matter can remain unmagnetized.

5. CONCLUSIONS

We have constructed a new model for the spreading of deflagration fronts during type I X-ray bursts. In contrast to previous models, we take into account the horizontal hydrodynamical flows arising as a result of the radial expansion of the burning atmosphere/ocean and the action of the Coriolis force due to rapid rotation typical for strongly accreting NSs in LMXBs. Our mechanism of heat transport relies on coherent hydrodynamical flows across the front that are set up as the fluid attains momentum balance, and it achieves speeds of front propagation in excess of tens of kilometers per second, necessary to account for the observed subsecond rise times of X-ray bursts. Previous workers invoked large-scale convective turbulence (on scales much larger than the vertical scale height) in order to obtain comparable front speeds. The speed of the front is analytically estimated in equation (24) for the case in which convective viscosity is not important and in equation (34) for the case in which the layers of the burning ocean are frictionally coupled (by, e.g., convection).

[14] It seems reasonable to assume that the small-scale magnetic field, with a coherence length of ~ 10 m (the ocean scale height), will not have a substantial effect on the large-scale (~ 1 km, roughly the width of the front) lateral shear.

In addition to the analytical arguments, we constructed and numerically evolved a two-layer shallow water model of the burning layers. Our simulations agree very well with our analytical estimates, and we found that the physics of propagation of geostrophically supported fronts is independent of the details of the heating function, as long as it is a single-peaked function of temperature. This agreement gives us confidence that our results are valid for models with more realistic microphysics.

We have outlined the behavior of global hydrodynamical flows in the NS atmosphere/ocean during the burst and showed that these flows may explain many of the features of observed bursts. The very short rise times of X-ray bursts are easily accounted for if the speed of the burning front is set by the requirement of geostrophic balance. The lack of burst oscillations in many bursts may be due to the fact that the speed of the burning front is very dependent on the location on the NS surface and favors rapid propagation along near-equatorial latitude bands that wipes out asymmetry, rather than simple spreading of a hot spot that maintains asymmetry. The rather large frequency drifts of burst oscillations in tails of some bursts can be accounted for only if the lift-up drift due to the radial expansion (Strohmayer et al. 1997; Cumming & Bildsten 2000; Cumming et al. 2002) is combined with the geostrophic drift due to zonal flows in the cooling wake of the burning front. We argue that the burning front will generate a strong ($\sim 10^9$ G) small-scale magnetic field and that this magnetic field will enforce a vertically rigid flow of the ocean in the wake of the burning front. The vertical rigidity of the flow explains the observed high degree of coherence of the burst oscillations during the cooling tails of bursts, after convection has subsided and can no longer account for the coherence. We conjecture that strong zonal currents during the burst may lead to the formation of vortices of the type observed in the atmospheres of giant planets. These vortices may be responsible for X-ray flux oscillations in the burst tail. In addition, we predict the presence of yet unobserved chirps during rises of bursts. Detection of such chirps (which could have been missed in previous observations because of the large frequency spans that they cover) will tell us about the details of burning front propagation, such as its velocity or the latitudinal extent of the surface of the star that is covered by nuclear burning.

Our model is incomplete in several respects. We showed that the burning front on a rotating NS is a site of strong vertical and horizontal differential shear and that this shear flow can transport entropy across the front. However, we omitted the small-scale mixing and heat diffusion, and thus we have not showed that this heat can indeed be delivered into the cold fuel, heat it up, and ignite it as the burning front propagates. Since flows with strong shear tend to have both local and global hydrodynamical instabilities, we are confident that such heat exchange does occur and is robust. Only two- or three-dimensional hydrodynamical simulations will be able to authoritatively settle this issue, and we have outlined how our results would be modified if the mixing exists but is not as efficient as we have assumed. In addition, such simulations will be useful for understanding the dynamical (frictional) coupling between the layers of the burning ocean, which, as we showed, has a substantial effect on the speed of propagation of the burning front. Finally, further modeling of the global nonaxisymmetric instabilities arising in the horizontal shear flows may confirm our con-

jecture of trapped vortices as the origin of flux modulation at late times during X-ray bursts.

In this paper we have demonstrated the usefulness of the shallow water model for understanding X-ray bursts. Two-dimensional simulations utilizing the shallow water model on a sphere will complement future vertically resolved hydrodynamical simulations and will allow us to generate realistic light curves and make more refined predictions of frequency behavior of burst oscillations.

APPENDIX A

FORMAL DERIVATION OF MODEL EQUATIONS

The shallow water equations (40)–(45) for incompressible fluid can be derived as a formal limit of the Euler equations for compressible fluid. This is useful for establishing the connection between the entropy sources in compressible fluid and mass sources which are used to simulate heating in the incompressible case. Using the continuity equation and the ideal gas law, the heat equation (39) can be rewritten as

$$(1 - \kappa) \frac{dT}{dt} = -\kappa T \mathbf{V} \cdot \boldsymbol{v} + \frac{J}{c_p} , \tag{A1}$$

where $\kappa = 1 - 1/\gamma$. In the limit of an incompressible fluid, $\gamma \to \infty$ and $\kappa \to 1$. We can then equate the right-hand side of equation (A1) to zero. We consider a layer of uniform temperature T_0 and height h, which in our model is equal to the scale height $c_p T_0/g$. Integrating equation (A1) in the vertical direction over the layer height, we get

$$h \mathbf{V}_{||} \cdot \boldsymbol{v} + (v_z|_{z=h} - v_z|_{z=0}) = \frac{J}{g} . \tag{A2}$$

We assume a hard surface at the bottom of the layer ($v_z|_{z=0} = 0$) and use $v_z|_{z=h} = dh/dt$ as the velocity of the surface. This yields the continuity equation as in equations (40)–(41) with effective mass source $Q = J/g$ representing heating. The momentum equations (42)–(45) directly follow from the Euler equations for a constant density layer in hydrostatic balance.

REFERENCES

Bhattacharya, D. 1995, J. Astrophys. Astron., 16, 217
Bildsten, L. 1995, ApJ, 438, 852
———. 1998, in The Many Faces of Neutron Stars, ed. R. Buccheri, J. van Paradijs, & M. A. Alpar (Dodrecht: Kluwer), 419
Chakrabarty, D., & Morgan, E. H. 1998, Nature, 394, 346
Chan, J. C. L., & Williams, R. T. 1987, J. Atmos. Sci., 44, 1257
Cumming, A., & Bildsten, L. 2000, ApJ, 544, 453
Cumming, A., Morsink, S. M., Bildsten, L., Friedman, J. L., & Holtz, D. E. 2002, ApJ, 564, 343
Fryxell, B. A., & Woosley, S. E. 1982a, ApJ, 258, 733
———. 1982b, ApJ, 261, 332
Fujimoto, M. Y. 1988, A&A, 198, 163
Fushiki, I., & Lamb, D. Q. 1987, ApJ, 317, 368
Galloway, D. K., Chakrabarty, D., Muno, M. P., & Savov, P. 2001, ApJ, 549, L85
Gill, A. E. 1982, Atmosphere-Ocean Dynamics (New York: Academic Press)
Hanawa, T., & Fujimoto, M. Y. 1984, PASJ, 36, 199
Hansen, C. J., & van Horn, H. M. 1975, ApJ, 195, 735
Holton, J. R. 1992, An Introduction to Dynamic Meteorology (San Diego: Academic Press)
Inogamov, N. A., & Sunyaev, R. A. 1999, Astron. Lett., 25, 269
Joss, P. C. 1977, Nature, 270, 310
Kluzniak, W., & Ruderman, M. 1998, ApJ, 508, L113
Lewin, W. H. G., van Paradijs, J., & Taam, R. E. 1995, in X-ray Binaries (Cambridge: Cambridge Univ. Press), 175–233
Maraschi, L., & Cavaliere, A. 1977, Highlights Astron., 4, 127

Miller, M. C. 1999, ApJ, 515, L77
———. 2000, ApJ, 537, 342
Muno, M. P., Chakrabarty, D., Galloway, D. K., & Savov, P. 2001, ApJ, 553, L157
Ooyama, K. 1969, J. Atmos. Sci., 26, 3
Pedlosky, J. 1987, Geophysical Fluid Dynamics (New York: Springer)
Psaltis, D., & Chakrabarty, D. 1999, ApJ, 521, 332
Romate, J. E. 1992, J. Comput. Phys., 99, 135
Ruderman, M. 1981, Prog. Part. Nucl. Phys., 6, 215
Sethian, J. A., & Vladimirsky, A. 2000, Proc. Natl. Acad. Sci., 97, 5699
Shara, M. M. 1982, ApJ, 261, 649
Smith, R. B., Li, X., & Wang, B. 1997, Tellus, 49A, 474
Spruit, H. C. 1999, A&A, 341, L1
Strohmayer, T. E. 2001, preprint (astro-ph/0012516)
Strohmayer, T. E., Jahoda, K., Giles, B. A., & Lee, U. 1997, ApJ, 486, 355
Strohmayer, T. E., Zhang, W., Swank, J. H., & Lapidus, I. 1998, ApJ, 503, L147
Thompson, K. W. 1987, J. Comput. Phys., 68, 1
van der Klis, M. 2000, ARA&A, 38, 717
van Straaten, S., van der Klis, M., Kuulkers, E., & Mendez, M. 2001, ApJ, 551, 907
Wijnands, R., Strohmayer, T., & Franco, L. 2001, ApJ, 549, L71
Wijnands, R., & van der Klis, M. 1998, ApJ, 507, L63
Williams, F. A. 1965, in Combustion Theory (Reading: Addison-Wesley), 175–177
Woosley, S. E., & Taam, R. E. 1976, Nature, 263, 101
Zingale, M., et al. 2001, ApJS, 133, 195